

Observations and three-dimensional ionization structure of the planetary nebula SuWt 2^{*}

A. Danehkar,¹† Q. A. Parker^{1,2} and B. Ercolano^{3,4}

¹Research Centre in Astronomy, Astrophysics & Astrophotonics, Macquarie University, Sydney, NSW 2109, Australia

²Australian Astronomical Observatory, PO Box 296, Epping, NSW 1710, Australia

³Universitäts-Sternwarte München, Ludwig-Maximilians Universität München, Scheinerstr 1, D-81679 München, Germany

⁴Excellence Cluster Universe, Boltzmannstr 2, D-85748 Garching, Germany

Accepted 2013 June 17. Received 2013 June 16; in original form 2013 March 20

ABSTRACT

The planetary nebula SuWt 2 (PN G311.0+02.4) is an unusual object with a prominent, inclined central emission ellipse and faint bipolar extensions. It has two A-type stars in a proven binary system at the centre. However, the radiation from these two central stars is too soft to ionize the surrounding material leading to a so far fruitless search for the responsible ionizing source. Such a source is clearly required and has already been inferred to exist via an observed temporal variation of the centre-of-mass velocity of the A-type stars. Moreover, the ejected nebula is nitrogen rich which raises question about the mass-loss process from a likely intermediate-mass progenitor. We use optical integral-field spectroscopy to study the emission lines of the inner nebula ring. This has enabled us to perform an empirical analysis of the optical collisionally excited lines, together with a fully three-dimensional photoionization modelling. Our empirical results are used to constrain the photoionization models, which determine the evolutionary stage of the responsible ionizing source and its likely progenitor. The time-scale for the evolutionary track of a hydrogen-rich model atmosphere is inconsistent with the dynamical age obtained for the ring. This suggests that the central star has undergone a very late thermal pulse. We conclude that the ionizing star could be hydrogen deficient and compatible with what is known as a PG 1159-type star. The evolutionary tracks for the very late thermal pulse models imply a central star mass of $\sim 0.64 M_{\odot}$, which originated from an $\sim 3 M_{\odot}$ progenitor. The evolutionary time-scales suggest that the central star left the asymptotic giant branch about 25 000 yr ago, which is consistent with the nebula's age.

Key words: ISM: abundances – planetary nebulae: individual: PN SuWt 2.

1 INTRODUCTION

The southern planetary nebula (PN) SuWt 2 (PN G311.0+02.4) is a particularly exotic object. It appears as an elliptical ring-like nebula with much fainter bipolar lobes extending perpendicularly to the ring, and with what appears to be an obvious, bright central star. The inside of the ring is apparently empty, but brighter than the nebula's immediate surroundings. An overall view of this ring-shaped structure and its surrounding environment can be seen in the $H\alpha$ image available from the SuperCOSMOS $H\alpha$ Sky Survey (Parker et al. 2005). West (1976) classified SuWt 2 as of intermediate excitation class (EC; $p = 6-7$; Aller & Liller 1968) based on the

strength of the $\text{He II } \lambda 4686$ and $[\text{O II}] \lambda 3728$ doublet lines. The line ratio of $[\text{N II}] \lambda 6584$ and $H\alpha$ illustrated by Smith, Bally & Walawender (2007) showed a nitrogen-rich nebula that most likely originated from post-main-sequence mass-loss of an intermediate-mass progenitor star.

Over a decade ago, Bond (2000) discovered that the apparent central star of SuWt 2 (NSV 19992) is a detached double-lined eclipsing binary consisting of two early A-type stars of nearly identical type. Furthermore, Bond et al. (2002) suggested that this is potentially a triple system consisting of the two A-type stars and a hot, unseen PN central star. However, to date, optical and UV studies have failed to find any signature of the nebula's true ionizing source (e.g. Bond et al. 2002; Bond, Pollacco & Webbink 2003; Exter et al. 2003, 2010). Hence, the putative hot (pre-)white dwarf would have to be in a wider orbit around the close eclipsing pair. Exter et al. (2010) recently derived a period of 4.91 d from time series photometry and spectroscopy of the eclipsing pair, and concluded that the centre-of-mass velocity of the central binary varies with time, based

^{*}Based on observations made with the Australian National University 2.3 m telescope at the Siding Spring Observatory under programmes 2090064 and 3120158.

†E-mail: ashkbiz.danehkar@mq.edu.au

on different systemic velocities measured over the period from 1995 to 2001. This suggests the presence of an unseen third orbiting body, which they concluded is a white dwarf of $\sim 0.7 M_{\odot}$, and is the source of ionizing radiation for the PN shell.

There is also a very bright B1Ib star, SAO 241302 (HD 121228), located 73 arcsec northeast of the nebula. Smith et al. (2007) speculated that this star is the ionizing source for SuWt 2. However, the relative strength of $\text{He II } \lambda 4686$ in our spectra (see later) shows that the ionizing star must be very hot, $T > 100\,000$ K, so the B1 star is definitively ruled out as the ionizing source.

Narrow-band $\text{H}\alpha + [\text{N II}]$ and $[\text{O III}] \lambda 5007$ images of SuWt 2 obtained by Schwarz, Corradi & Melnick (1992) show that the angular dimensions of the bright elliptical ring are about $86.5 \text{ arcsec} \times 43.4 \text{ arcsec}$ at the 10 percent of maximum surface brightness isophote (Tylenda et al. 2003), and are used throughout this paper. Smith et al. (2007) used the MOSAIC2 camera on the Cerro Tololo Inter-American Observatory (CTIO) 4 m telescope to obtain a more detailed $\text{H}\alpha + [\text{N II}]$ image, which hints that the ring is possibly the inner edge of a swept-up disc. The $[\text{N II}]$ image also shows the bright ring structure and much fainter bipolar lobes extending perpendicular to the ring plane. We can see similar structure in the images taken by Bond and Exter in 1995 with the CTIO 1.5 m telescope using an $\text{H}\alpha + [\text{N II}]$ filter. Fig. 1 shows both narrow-band $[\text{N II}] \lambda 6584 \text{ \AA}$ and $\text{H}\alpha$ images taken in 1995 with the ESO 3.6 m New Technology Telescope at the La Silla Paranal Observatory using the ESO Multi-Mode Instrument (EMMI). The long-slit emission-line spectra also obtained with the EMMI (programme ID 074.D-0373) in 2005 revealed much more detail of the nebular morphology. The first spatio-kinematical model using the EMMI long-slit data by Jones et al. (2010) suggested the existence of a bright torus with a systemic heliocentric radial velocity of $-25 \pm 5 \text{ km s}^{-1}$ encircling the waist of an extended bipolar nebular shell.

In this paper, we aim to uncover the properties of the hidden hot ionizing source in SuWt 2. We aim to do this by applying a self-consistent three-dimensional photoionization model using the *MOCASSIN 3D* code by Ercolano et al. (2003a, 2008) and Ercolano, Barlow & Storey (2005). In Section 2, we describe our optical integral-field observations as well as the data reduction process and the corrections for interstellar extinction. In Section 3, we describe the kinematics. In Section 4, we present our derived electron temperature and density, together with our empirical ionic abundances in Section 5. In Section 6, we present derived ionizing source properties and distance from our self-consistent photoionization models, followed by a conclusion in Section 7.

2 OBSERVATIONS AND DATA REDUCTION

Integral-field spectra of SuWt 2 were obtained during two observing runs in 2009 May and 2012 August with the Wide-Field Spectrograph (WiFeS; Dopita et al. 2007). WiFeS is an image-slicing integral field unit developed and built for the ANU 2.3 m telescope at the Siding Spring Observatory, feeding a double-beam spectrograph. WiFeS samples 0.5 arcsec along each of twenty-five $38 \text{ arcsec} \times 1 \text{ arcsec}$ slits, which provides a field of view of $25 \text{ arcsec} \times 38 \text{ arcsec}$ and a spatial resolution element of $1.0 \text{ arcsec} \times 0.5 \text{ arcsec}$ (or $1 \text{ arcsec} \times 1 \text{ arcsec}$ for y-binning = 2). The spectrograph uses volume phase holographic gratings to provide a spectral resolution of $R = 3000$ (100 km s^{-1} full width at half-maximum, FWHM) and $R = 7000$ (45 km s^{-1} FWHM) for the red and blue arms, respectively. Each grating has a different wavelength coverage. It can operate two data accumulation modes: classical and nod-and-shuffle (N&S). The N&S mode accumulates

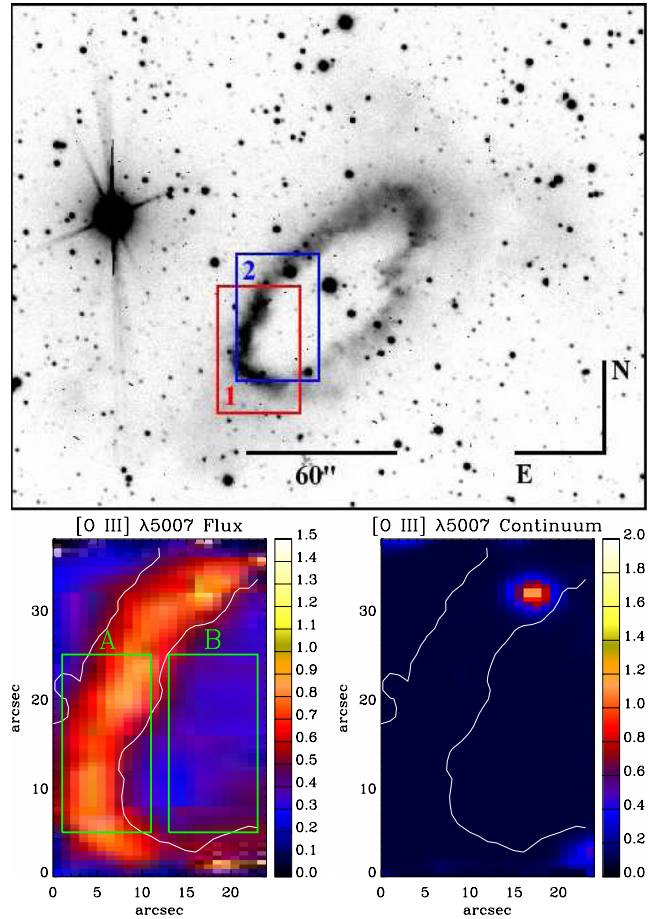


Figure 1. Top panel: narrow-band filter image of the PN SuWt 2 on a logarithmic scale in $\text{H}\alpha$ and $[\text{N II}] \lambda 6584 \text{ \AA}$ taken with the European Southern Observatory (ESO) 3.6 m telescope (programme ID 055.D-0550). The rectangles correspond to the WiFeS fields of view used for our study: 1 (red) and 2 (blue); see Table 1 for more details. Bottom panels: spatial distribution maps of flux intensity and continuum of $[\text{O III}] \lambda 5007$ for field 2 and locations of apertures ($10 \text{ arcsec} \times 20 \text{ arcsec}$) used to integrate fluxes, namely ‘A’ the ring and ‘B’ the interior structure. The white contour lines show the distribution of the above narrow-band $\text{H}\alpha$ emission in arbitrary units. North is up and east is towards the left-hand side.

both object and nearby sky-background data in either equal exposures or unequal exposures. The complete performance of the WiFeS has been fully described by Dopita et al. (2007, 2010).

Our observations were carried out with the B3000/R3000 grating combination and the RT 560 dichroic using N&S mode in 2012 August, and the B7000/R7000 grating combination and the RT 560 dichroic using the classical mode in 2009 May. This covers $\lambda\lambda 3300\text{--}5900 \text{ \AA}$ in the blue channel and $\lambda\lambda 5500\text{--}9300 \text{ \AA}$ in the red channel. As summarized in Table 1, we took two different WiFeS exposures from different positions of SuWt 2; see Fig. 1 (top). The sky field was collected about 1 arcmin away from the object. To reduce and calibrate the data, it is necessary to take the usual bias frames, dome flat-field frames, twilight sky flats, ‘wire’ frames and arc calibration lamp frames. Although wire, arc, bias and dome flat-field frames were collected during the afternoon prior to observing, arc and bias frames were also taken through the night. Twilight sky flats were taken in the evening. For flux calibration, we also observed some spectrophotometric standard stars.

Table 1. Journal of SuWt 2 observations at the ANU 2.3 m telescope.

Field	1	2
Instrument	WiFeS	WiFeS
Wavelength resolution	~7000	~3000
Wavelength range (Å)	4415–5589, 5222–7070	3292–5906, 5468–9329
Mode	Classical	N&S
y-binning	1	2
Object exposure (s)	900	1200
Sky exposure (s)	–	600
Standard star	LTT 3218	LTT 9491, HD 26169
v_{LSR} correction	–5.51	–25.77
Airmass	1.16	1.45
Position (see Fig. 1)	13:55:46.2 –59:22:57.9	13:55:45.5 –59:22:50.3
Date (UTC)	16/05/09	20/08/12

2.1 WiFeS data reduction

The WiFeS data were reduced using the `WIFES` pipeline (updated on 2011 November 21), which is based on the Gemini `IRAF`¹ package (version 1.10; `IRAF` version 2.14.1) developed by the Gemini Observatory for the integral-field spectroscopy.

Each CCD pixel in the WiFeS camera has a slightly different sensitivity, giving pixel-to-pixel variations in the spectral direction. This effect is corrected using the dome flat-field frames taken with a quartz iodine (QI) lamp. Each slitlet is corrected for slit transmission variations using the twilight sky frame taken at the beginning of the night. The wavelength calibration was performed using Ne–Ar arc exposures taken at the beginning of the night and throughout the night. For each slitlet, the corresponding arc spectrum is extracted, and then wavelength solutions for each slitlet are obtained from the extracted arc lamp spectra using low-order polynomials. The spatial calibration was accomplished by using so-called ‘wire’ frames obtained by diffuse illumination of the coronagraphic aperture with a QI lamp. This procedure locates only the centre of each slitlet, since small spatial distortions by the spectrograph are corrected by the WiFeS cameras. Each wavelength slice was also corrected for the differential atmospheric refraction by relocating each slice in x and y to its correct spatial position.

In the N&S mode, the sky spectra are accumulated in the unused 80 pixel spaces between the adjacent object slices. The sky subtraction is conducted by subtracting the image shifted by 80 pixels from the original image. The cosmic rays and bad pixels were removed from the raw data set prior to sky subtraction using the `IRAF` task `LACOS_IM` of the cosmic ray identification procedure of van Dokkum (2001), which is based on a Laplacian edge detection algorithm. However, a few bad pixels and cosmic rays still remained in raw data, and these were manually removed by the `IRAF/STSDAS` task `IMEDIT`.

We calibrated the science data to absolute flux units using observations of spectrophotometric standard stars observed in classical mode (no N&S), so sky regions within the object data cube were used for sky subtraction. An integrated flux standard spectrum is created by summing all spectra in a given aperture. After manually removing absorption features, an absolute calibration curve is fitted

to the integrated spectrum using third-order polynomials. The flux calibration curve was then applied to the object data to convert to an absolute flux scale. The [O I] $\lambda 5577$ Å night sky line was compared in the sky spectra of the red and blue arms to determine a difference in the flux levels, which was used to scale the blue spectrum of the science data. Our analysis using different spectrophotometric standard stars (LTT 9491 and HD 26169) revealed that the spectra at the extreme blue have an uncertainty of about 30 per cent and are particularly unreliable for faint objects due to the CCD’s poor sensitivity in this area.

2.2 Nebular spectrum and reddening

Table 2 represents a full list of observed lines and their measured fluxes from different apertures (10 arcsec \times 20 arcsec) taken from field 2: (A) the ring and (B) the inside of the shell. Fig. 1 (bottom panel) shows the location and area of each aperture in the nebula. The top and bottom panels of Fig. 2 show the extracted blue and red spectra after integration over the aperture located on the ring with the strongest lines truncated so the weaker features can be seen. The emission-line identification, laboratory wavelength, multiplet number, the transition with the lower and upper spectral terms are given in columns 1–4 of Table 2, respectively. The observed fluxes of the interior and ring, and the fluxes after correction for interstellar extinction are given in columns 5–8. Columns 9 and 10 present the integrated and dereddened fluxes after integration over two apertures (A and B). All fluxes are given relative to $H\beta$, on a scale where $H\beta = 100$.

For each spatially resolved emission-line profile, we extracted flux intensity, central wavelength (or centroid velocity) and FWHM (or velocity dispersion). Each emission-line profile for each spaxel is fitted to a single Gaussian curve using the `MPFIT` routine (Markwardt 2009), an IDL version of the `MINPACK-1` FORTRAN code (Moré 1977), which applies the Levenberg–Marquardt technique to the non-linear least-squares problem. Flux intensity maps of key emission lines of field 2 are shown in Fig. 3 for [O III] $\lambda 5007$, $H\alpha$ $\lambda 6563$, [N II] $\lambda 6584$ and [S II] $\lambda 6716$; the same ring morphology is visible in the [N II] map as seen in Fig. 1. White contour lines in the figures depict the distribution of the narrow-band emission of $H\alpha$ and [N II] taken with the ESO 3.6 m telescope, which can be used to distinguish the borders between the ring structure and the inside region. We excluded the stellar continuum offset from the final flux maps using `MPFIT`, so spaxels show only the flux intensities of the nebulae.

The $H\alpha$ and $H\beta$ Balmer emission-line fluxes were used to derive the logarithmic extinction at $H\beta$, $c(H\beta) = \log [I(H\beta)/F(H\beta)]$, for the theoretical line ratio of the case B recombination ($T_e = 10\,000$ K and $N_e = 100\text{ cm}^{-3}$; Hummer & Storey 1987). Each flux at the central wavelength was corrected for reddening using the logarithmic extinction $c(H\beta)$ according to

$$I(\lambda) = F(\lambda) 10^{c(H\beta)[1+f(\lambda)]}, \quad (1)$$

where $F(\lambda)$ and $I(\lambda)$ are the observed and intrinsic line flux, respectively, and $f(\lambda)$ is the standard Galactic extinction law for a total-to-selective extinction ratio of $R_V \equiv A(V)/E(B - V) = 3.1$ (Seaton 1979a,b; Howarth 1983).

Accordingly, we obtained an extinction of $c(H\beta) = 0.64 [E(B - V) = 0.44]$ for the total fluxes (column 9 in Table 2). Our derived nebular extinction is in good agreement with the value found by Exter et al. (2010), $E(B - V) = 0.40$ for the central star, though they obtained $E(B - V) = 0.56$ for the nebula. It may point to the fact that all reddening is not due to the interstellar medium (ISM), and there is some dust contribution in the nebula. Adopting a total

¹ The Image Reduction and Analysis Facility (`IRAF`) software is distributed by the National Optical Astronomy Observatory.

Table 2. Observed and dereddened relative line fluxes, on a scale where $H\beta = 100$. The integrated observed $H(\beta)$ flux was dereddened using $c(H\beta)$ to give an integrated dereddened flux. Uncertain (errors of 20 per cent) and very uncertain (errors of 30 per cent) values are followed by ‘:’ and ‘::’, respectively. The symbol ‘*’ denotes doublet emission lines.

Region			Interior		Ring		Total		
line	$\lambda_{\text{lab}}(\text{\AA})$	Mult	Transition	$F(\lambda)$	$I(\lambda)$	$F(\lambda)$	$I(\lambda)$	$F(\lambda)$	$I(\lambda)$
(1)	(2)	(3)	(4)	(5)	(6)	(7)	(8)	(9)	(10)
3726 [O II]	3726.03	F1	$2p^3\ ^4S_{3/2}-2p^3\ ^2D_{3/2}$	183 ± 54	307 ± 91	576 ± 172	815 ± 244	479 ± 143	702 ± 209
3729 [O II]	3728.82	F1	$2p^3\ ^4S_{3/2}-2p^3\ ^2D_{5/2}$	*	*	*	*	*	*
3869 [Ne III]	3868.75	F1	$2p^4\ ^3P_2-2p^4\ ^1D_2$	128.93::	199.42::	144.31::	195.22::	145.82::	204.57::
3967 [Ne III]	3967.46	F1	$2p^4\ ^3P_1-2p^4\ ^1D_2$	–	–	15.37::	20.26::	–	–
4102 H δ	4101.74	H6	$2p^2P-6d^2D$	–	–	16.19:	20.55:	16.97:	22.15:
4340 H γ	4340.47	H5	$2p^2P-5d^2D$	24.47::	31.10::	30.52:	36.04:	31.69:	38.18:
4363 [O III]	4363.21	F2	$2p^2\ ^1D_2-2p^2\ ^1S_0$	37.02::	46.58::	5.60	6.57	5.15	6.15
4686 He II	4685.68	3-4	$3d^2D-4f^2F$	80.97	87.87	29.98	31.72	41.07	43.76
4861 H β	4861.33	H4	$2p^2P-4d^2D$	100.00	100.00	100.00	100.00	100.00	100.00
4959 [O III]	4958.91	F1	$2p^2\ ^3P_1-2p^2\ ^1D_2$	390.90	373.57	173.63	168.27	224.48	216.72
5007 [O III]	5006.84	F1	$2p^2\ ^3P_2-2p^2\ ^1D_2$	1347.80	1259.76	587.22	560.37	763.00	724.02
5412 He II	5411.52	4-7	$4f^2F-7g^2G$	19.33	15.01	5.12	4.30	6.90	5.68
5755 [N II]	5754.60	F3	$2p^2\ ^1D_2-2p^2\ ^1S_0$	7.08:	4.90:	13.69	10.61	10.17	7.64
5876 He I	5875.66	V11	$2p^3P-3d^3D$	–	–	11.51	8.69	8.96	6.54
6548 [N II]	6548.10	F1	$2p^2\ ^3P_1-2p^2\ ^1D_2$	115.24	63.13	629.36	414.79	513.64	321.94
6563 H α	6562.77	H3	$2p^2P-3d^2D$	524.16	286.00	435.14	286.00	457.70	286.00
6584 [N II]	6583.50	F1	$2p^2\ ^3P_2-2p^2\ ^1D_2$	458.99	249.05	1980.47	1296.67	1642.12	1021.68
6678 He I	6678.16	V46	$2p^1P_1-3d^1D_2$	–	–	3.30	2.12	2.68	1.63
6716 [S II]	6716.44	F2	$3p^3\ ^4S_{3/2}-3p^3\ ^2D_{5/2}$	60.63	31.77	131.84	84.25	116.21	70.36
6731 [S II]	6730.82	F2	$3p^3\ ^4S_{3/2}-3p^3\ ^2D_{3/2}$	30.08	15.70	90.39	57.61	76.98	46.47
7005 [Ar V]	7005.40	F1	$3p^2\ ^3P-3p^2\ ^1D$	5.46:	2.66:	–	–	–	–
7136 [Ar III]	7135.80	F1	$3p^4\ ^3P_2-3p^4\ ^1D_2$	31.81	15.03	26.22	15.59	27.75	15.51
7320 [O II]	7319.40	F2	$2p^3\ ^2D_{5/2}-2p^3\ ^2P$	18.84	8.54	9.00	5.20	10.96	5.93
7330 [O II]	7329.90	F2	$2p^3\ ^2D_{3/2}-2p^3\ ^2P$	12.24	5.53	4.50	2.60	6.25	3.37
7751 [Ar III]	7751.43	F1	$3p^4\ ^3P_1-3p^4\ ^1D_2$	46.88	19.38	10.97	5.95	19.05	9.60
9069 [S III]	9068.60	F1	$3p^2\ ^3P_1-3p^2\ ^1D_2$	12.32	4.07	13.27	6.16	13.34	5.65
$c(H\beta)$				–	0.822	–	0.569	–	0.638

observed flux value of $\log F(H\alpha) = -11.69 \text{ erg cm}^{-2} \text{ s}^{-1}$ for the ring and interior structure (Frew 2008; Frew, Bojčić & Parker 2013a; Frew et al. 2013b) and using $c(H\beta) = 0.64$ lead to the dereddened $H\alpha$ flux of $\log I(H\alpha) = -11.25 \text{ erg cm}^{-2} \text{ s}^{-1}$.

According to the strength of He II $\lambda 4686$ relative to $H\beta$, the PN SuWt 2 is classified as the intermediate excitation class with $EC = 6.6$ (Dopita & Meatheringham 1990) or $EC = 7.8$ (Reid & Parker 2010). The EC is an indicator of the central star effective temperature (Dopita & Meatheringham 1991; Reid & Parker 2010). Using the $T_{\text{eff}}-EC$ relation of Magellanic Cloud PNe found by Dopita & Meatheringham (1991), we estimate $T_{\text{eff}} = 143 \text{ kK}$ for $EC = 6.6$. However, we get $T_{\text{eff}} = 177 \text{ kK}$ for $EC = 7.8$ according to the transformation given by Reid & Parker (2010) for Large Magellanic Cloud PNe.

3 KINEMATICS

Fig. 4 presents maps of the flux intensity and the local standard of rest (LSR) radial velocity derived from the Gaussian profile fits for the emission line [N II] $\lambda 6584 \text{ \AA}$. We transferred the observed velocity v_{obs} to the LSR radial velocity v_{lsr} by determining the radial velocities induced by the motions of the Earth and Sun using the IRAF/ASTUTIL task RVCORRECT. The emission-line profile is also resolved if its velocity dispersion is wider than the instrumental width σ_{ins} . The instrumental width can be derived from the [O I] $\lambda 5577 \text{ \AA}$ and $\lambda 6300 \text{ \AA}$ night sky lines; it is typically $\sigma_{\text{ins}} \approx 42 \text{ km s}^{-1}$ for $R \sim 3000$ and $\sigma_{\text{ins}} \approx 19 \text{ km s}^{-1}$ for $R \sim 7000$. Fig. 4 (right) shows the variation of the LSR radial velocity in the

south-east side of the nebula. We see that the radial velocity decreases as moving anticlockwise on the ellipse. It has a low value of about $-70 \pm 30 \text{ km s}^{-1}$ on the west co-vertex of the ellipse and a high value of $-50 \pm 25 \text{ km s}^{-1}$ on the south vertex. This variation corresponds to the orientation of this nebula, namely the inclination and projected nebula on the plane of the sky. It obviously implies that the east side moves towards us, while the west side escapes from us.

Kinematic information of the ring and the central star is summarized in Table 3. Jones et al. (2010) implemented a morphokinematic model using the modelling program SHAPE (Steffen & López 2006) based on the long-slit emission-line spectra at the high resolution of $R \sim 40000$, which is much higher than the moderate resolution of $R \sim 3000$ in our observations. They obtained the nebular expansion velocity of $v_{\text{exp}} = 28 \text{ km s}^{-1}$ and the LSR systemic velocity of $v_{\text{sys}} = -29.5 \pm 5$ at the best-fitting inclination of $i = 68^\circ \pm 2^\circ$ between the line of sight and the nebular axisymmetry axis. We notice that the nebular axisymmetric axis has a position angle of $PA = 48^\circ$ projected on to the plane of the sky, and measured from the north towards the east in the equatorial coordinate system (ECS). Transferring the PA in the ECS to the PA in the Galactic coordinate system yields the Galactic position angle of $GPA = 62^\circ 16'$, which is the PA of the nebular axisymmetric axis projected on to the plane of the sky, measured from the North Galactic Pole (NGP; $GPA = 0^\circ$) towards the Galactic east ($GPA = 90^\circ$). We notice an angle of $-27^\circ 44'$ between the nebular axisymmetric axis projected on to the plane of the sky and the Galactic plane. Fig. 5 shows the flux ratio map for the [S II] doublet to the H α recombination line

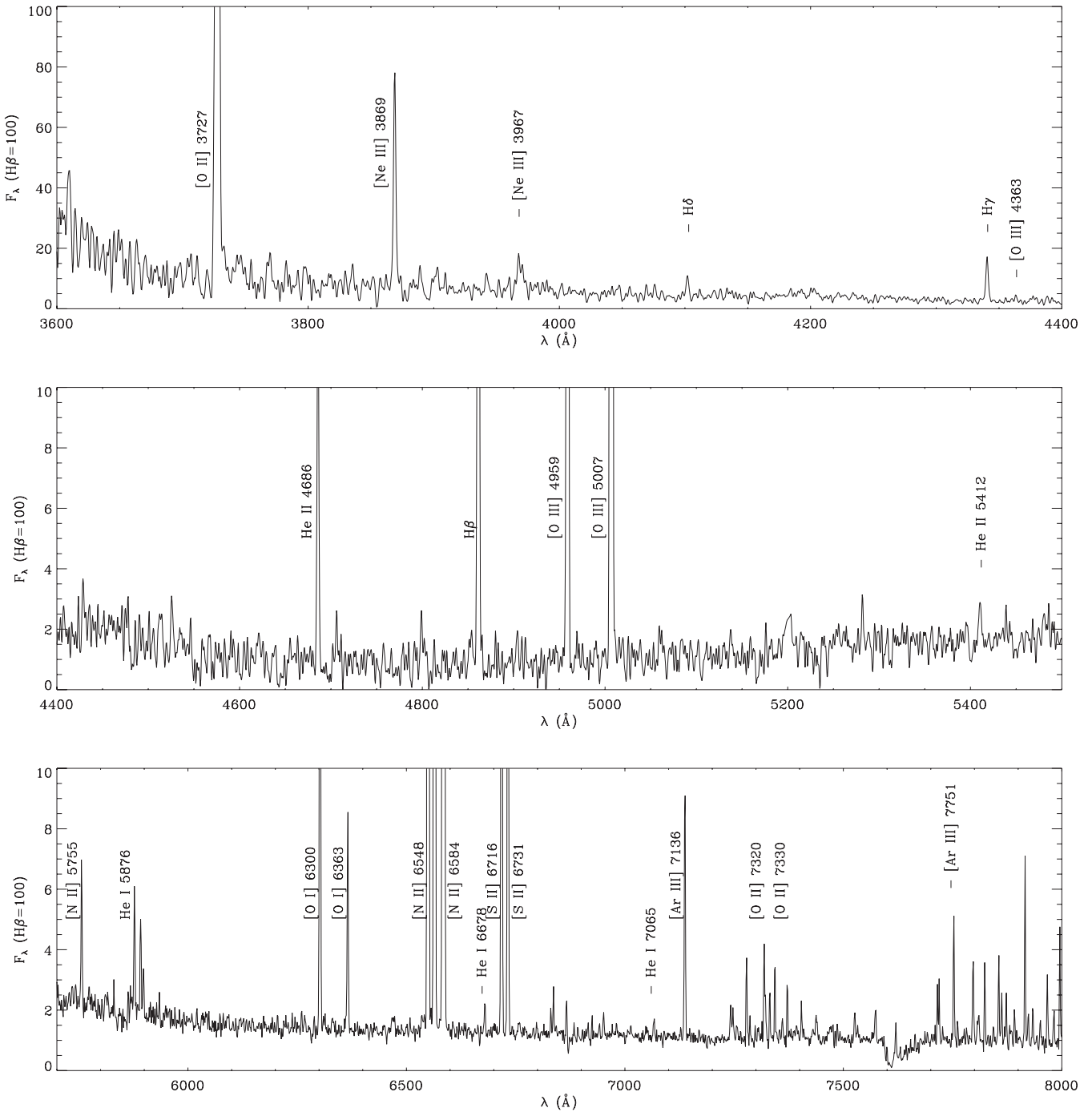


Figure 2. The observed optical spectrum from an aperture $10 \text{ arcsec} \times 20 \text{ arcsec}$ taken from field 2 located on the east ring of the PN SuWt 2 and normalized such that $F(\text{H}\beta) = 100$.

emission. The shock criterion $[\text{S II}] \lambda\lambda 6716, 6731/\text{H}\alpha \geq 0.5$ indicates the presence of a shock-ionization front in the ring. Therefore, the brightest south-east side of the nebula has a signature of an interaction with ISM.

The PPMXL catalogue² (Roeser, Demleitner & Schilbach 2010) reveals that the A-type stars of SuWt 2 move with the proper motion of $v_l = D\mu_l \cos(b) = (-8.09 \pm 8.46)D \text{ km s}^{-1}$ and $v_b = D\mu_b = (11.79 \pm 8.82)D \text{ km s}^{-1}$, where D is its distance in kpc.

They correspond to the magnitude of $v_{\mu} = (14.30 \pm 8.83)D \text{ km s}^{-1}$. Assuming a distance of $D = 2.3 \text{ kpc}$ (Exter et al. 2010) and $v_{\text{sys}} = -29.5 \pm 5 \text{ km s}^{-1}$ (LSR; Jones et al. 2010), this PN moves in the Cartesian Galactocentric frame with peculiar (non-circular) velocity components of $(U_s, V_s, W_s) = (35.4 \pm 18.4, 11.0 \pm 13.7, 33.18 \pm 26.4) \text{ km s}^{-1}$, where U_s is towards the Galactic centre, V_s in the local direction of Galactic rotation and W_s towards the NGP (see Reid et al. 2009, peculiar motion calculations in their appendix). We see that SuWt 2 moves towards the NGP with $W_s = 33.18 \text{ km s}^{-1}$, and there is an interaction with ISM in the direction of its motion, i.e. the east side of the nebula.

² Website: <http://vo.uni-hd.de/ppmxl>

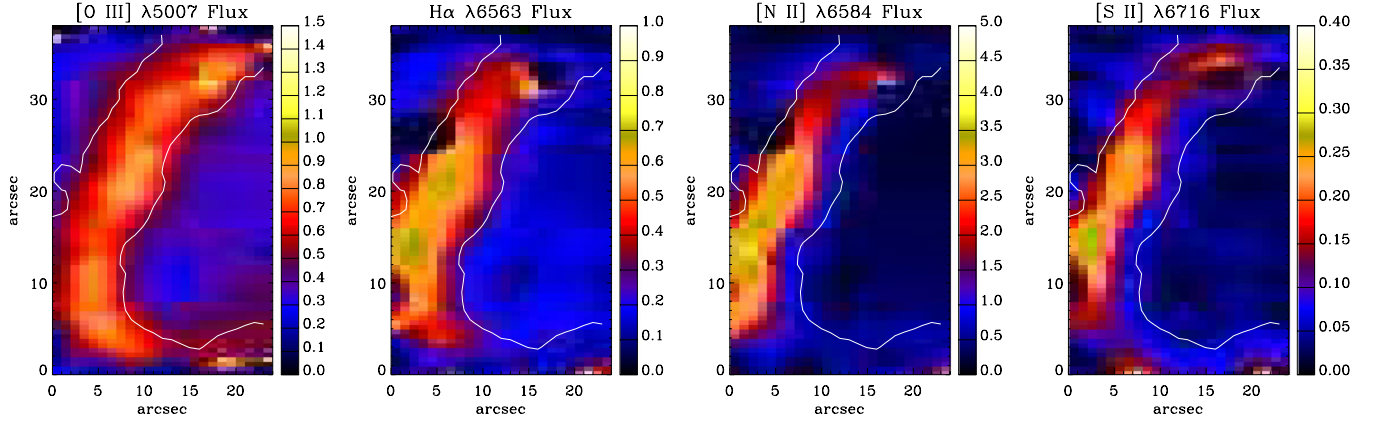


Figure 3. Underreddened flux maps for field 2 (see Fig. 1) of the PN SuWt 2: [O III] $\lambda 5007$, $H\alpha$ $\lambda 6563$, [N II] $\lambda 6584$ and [S II] $\lambda 6716$ Å. The flux is derived from single-Gaussian profile fits to the emission line at each spaxel. The white contour lines show the distribution of the narrow-band emission of $H\alpha$ and [N II] in arbitrary units taken with the ESO 3.6 m telescope. North is up and east is towards the left-hand side. Flux unit is in 10^{-15} erg s^{-1} cm^{-2} spaxel $^{-1}$.

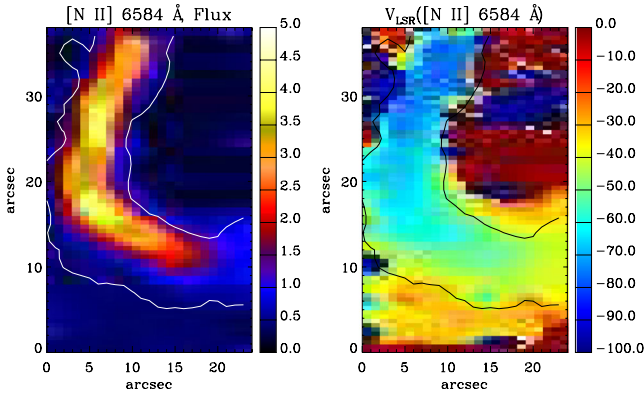


Figure 4. Flux intensity and radial velocity (V_{LSR}) map in [N II] $\lambda 6584$ Å for field 1 (see Table 1) of the PN SuWt 2. The white/black contour lines show the distribution of the narrow-band emission of $H\alpha$ and [N II] in arbitrary units taken with the ESO 3.6 m telescope. North is up and east is towards the left-hand side. Units are in $km s^{-1}$.

Table 3. Kinematic parameters on the SuWt 2's ring and its central star.

Parameter	Value
$a = r$ (outer radius)	45 ± 4 arcsec
$b = r \cos i$	17 ± 2 arcsec
Thickness	13 ± 2 arcsec
PA	$48^\circ \pm 2^\circ$
GPA	$62^\circ 16' \pm 2^\circ$
Inclination (i)	$68^\circ \pm 2^\circ$
v_{sys} (LSR)	-29.5 ± 5 $km s^{-1}$
v_{exp}	28 ± 5 $km s^{-1}$

We notice a very small peculiar velocity ($V_s = 11$ $km s^{-1}$) in the local direction of Galactic rotation, so a kinematic distance may also be estimated as the Galactic latitude is a favourable one for such a determination. We used the `FORTAN` code for the ‘revised’ kinematic distance prescribed in Reid et al. (2009), and adopted the IAU standard parameters of the Milky Way, namely the distance to the Galactic centre $R_0 = 8.5$ kpc and a circular rotation speed $\Theta_0 = 220$ $km s^{-1}$ for a flat rotation curve ($d\Theta/dR = 0$), and the solar motion of $U_\odot = 10.30$ $km s^{-1}$, $V_\odot = 15.3$ $km s^{-1}$ and $W_\odot = 7.7$ $km s^{-1}$. The LSR systemic velocity of -29.5 $km s^{-1}$ (Jones et al.

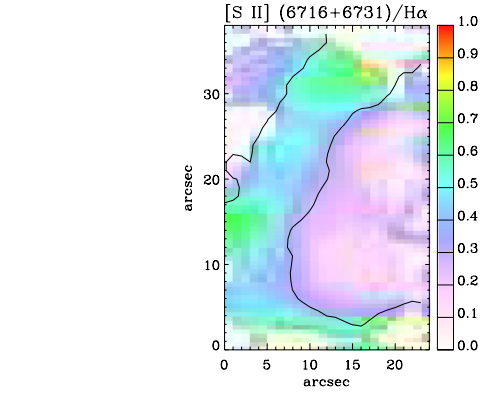


Figure 5. Flux ratio maps of the [S II] $\lambda 6716+6731$ Å to the $H\alpha$ recombination line emission.

2010) gives a kinematic distance of 2.26 kpc, which is in quite good agreement with the distance of 2.3 ± 0.2 kpc found by Exter et al. (2010) based on an analysis of the double-lined eclipsing binary system. This distance implies that SuWt 2 is in the tangent of the Carina–Sagittarius spiral arm of the Galaxy ($l = 311^\circ 0$, $b = 2^\circ 4$). Our adopted distance of 2.3 kpc means the ellipse’s major radius of 45 arcsec corresponds to a ring radius of $r = 0.47 \pm 0.04$ pc. The expansion velocity of the ring then yields a dynamical age of $\tau_{dyn} = r/v_{exp} = 17\,500 \pm 1560$ yr, which is defined as the radius divided by the constant expansion velocity. Nonetheless, the true age is more than the dynamical age, since the nebula expansion velocity is not constant through the nebula evolution. Dopita et al. (1996) estimated the true age typically around 1.5 of the dynamical age, so we get $\tau_{true} = 26\,250 \pm 2330$ yr for SuWt 2. If we take the asymptotic giant branch (AGB) expansion velocity of $v_{AGB} = v_{exp}/2$ (Gesicki & Zijlstra 2000), as the starting velocity of the new evolving PN, we also estimate the true age as $\tau_{true} = 2r/(v_{exp} + v_{AGB}) = 23\,360 \pm 2080$ yr.

4 PLASMA DIAGNOSTICS

We derived the nebular electron temperatures T_e and densities N_e from the intensities of the collisionally excited lines (CELs) by solving the equilibrium equations for an n -level atom (≥ 5) using `EQUIB`, a `FORTAN` code originally developed by Howarth & Adams (1981). Recently, it has been converted to `FORTAN 90`, and combined

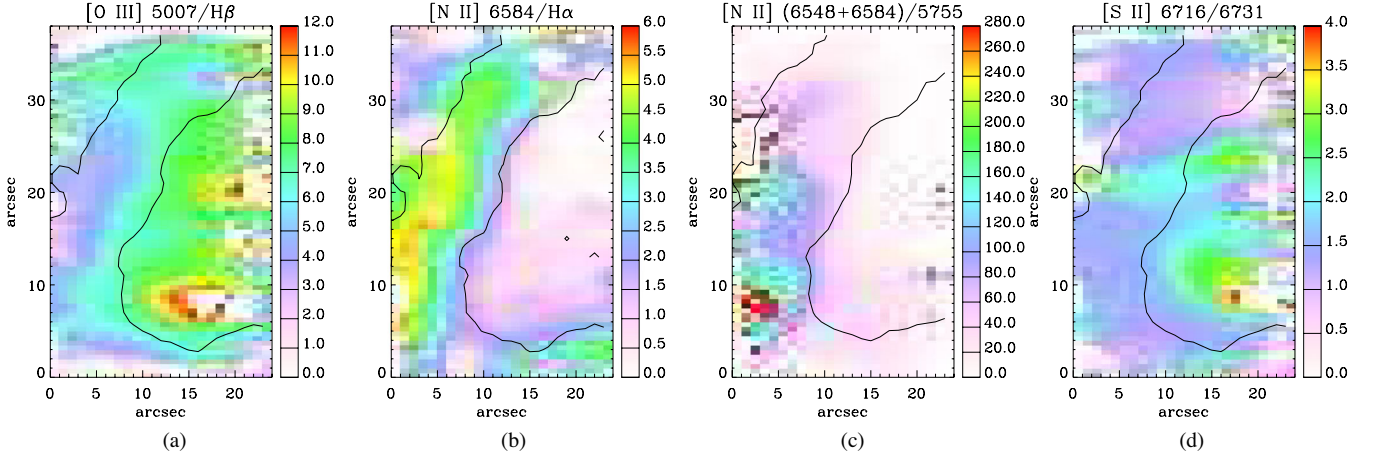


Figure 6. Flux ratio maps for field 2 (see Fig. 1) of the PN SuWt 2. From left to right: (a) flux ratio maps of the [O III] $\lambda 5007 \text{ \AA}$ to the $H\beta$ recombination line emission, (b) flux ratio map of the [N II] $\lambda 6584$ to the $H\alpha$ recombination line emission, (c) flux ratio map for the temperature-sensitive [N II] $\lambda\lambda 5755, 6548, 6583$ lines, and (d) for the density-sensitive [S II] doublet. The black contour lines show the distribution of the narrow-band emission of $H\alpha$ and [N II] in arbitrary units taken with the ESO 3.6 m telescope observations.

into simpler routines for NEAT (Wesson, Stock & Scicluna 2012). The atomic data sets used for our plasma diagnostics, as well as for the CEL abundance determination in Section 5, are the same as those used by Wesson et al. (2012).

The diagnostics procedure was as follows: we assumed a representative initial electron temperature of 10 000 K in order to derive $N_e([S II])$; then $T_e([N II])$ was derived in conjunction with the mean density derived from $N_e([S II])$. The calculations were iterated to give self-consistent results for N_e and T_e . The correct choice of electron density and temperature is essential to determine ionic abundances.

Fig. 6 shows flux ratio maps for the density-sensitive [S II] doublet. It indicates the electron density N_e of about $\lesssim 100 \text{ cm}^{-3}$ in the ring. We see that the interior region has an [S II] $\lambda\lambda 6716/6731$ flux ratio of more than 1.4, which means the inside of the ring has a very low density ($N_e \lesssim 50 \text{ cm}^{-3}$). Flux ratio maps for the temperature-sensitive [N II] $\lambda\lambda 5755, 6548, 6583$ lines indicate that the electron temperature T_e varies from 7000 to 14 000 K. As shown in Fig. 6, the brightest part of the ring in [N II] $\lambda 6584 \text{ \AA}$ has an electron temperature of about 8000 K. The inside of the ring has a mean electron temperature of about 11 800 K. We notice that Smith et al. (2007) found $N_e = 90 \text{ cm}^{-3}$ and $T_e = 11 400 \text{ K}$ using the R-C Spectrograph ($R \sim 6000$) on the CTIO 4 m telescope, though they obtained them from a 0.8 arcsec slit oriented along the major axis of the ring ($PA = 135^\circ$).

Table 4 lists the electron density (N_e) and the electron temperature (T_e) of the different regions, together with the ionization potential required to create the emitting ions. We see that the east part of the ring has a mean electron density of $N_e([S II]) \lesssim 100 \text{ cm}^{-3}$ and mean temperatures of $T_e([N II]) = 8140 \text{ K}$ and $T_e([O III]) = 12 390 \text{ K}$, while the less dense region inside the ring shows a high mean temperature of $T_e([N II]) = 11 760 \text{ K}$ and $T_e([O III])$ less than 20 000 K. We point out that the [S II] $\lambda\lambda 6716/6731$ line ratio of more than 1.40 is associated with the low-density limit of $N_e < 100 \text{ cm}^{-3}$, and we cannot accurately determine the electron density less than this limit (see e.g. A 39; Jacoby, Ferland & Korista 2001). Furthermore, we cannot resolve the [O II] $\lambda\lambda 3726, 3729$ doublet with our moderate spectral resolution ($R \sim 3000$). Plasma diagnostics indicates that the interior region is much hotter than the ring region. This implies the presence of a hard ionizing source located at the centre. It is worth to mention that $T_e([N II])$ is more appropriate

for singly ionized species, while $T_e([O III])$ is associated with doubly and more ionized species. Kingsburgh & Barlow (1994) found that $T_e([O III])/T_e([N II]) = 1.25$ for medium-excitation PNe and $T_e([O III])/T_e([N II]) = 1.15 + 0.0037 I(4686)$ for high-excitation PNe. Here, we notice that $T_e([O III])/T_e([N II]) = 1.52$ for the ring and $T_e([O III])/T_e([N II]) = 1.39$ for the total flux.

5 IONIC AND TOTAL ABUNDANCES

We derived ionic abundances for SuWt 2 using the observed CELs and the optical recombination lines (ORLs). We determined abundances for ionic species of N, O, Ne, S and Ar from CELs. In our determination, we adopted the mean $T_e([O III])$ and the upper limit of $N_e([S II])$ obtained from our empirical analysis in Table 4. Solving the equilibrium equations, using EQUIB, yields level populations and line sensitivities for given T_e and N_e . Once the level populations are solved, the ionic abundances, X^{i+}/H^+ , can be derived from the observed line intensities of CELs. We determined ionic abundances for He from the measured intensities of ORLs using the effective recombination coefficients from Storey & Hummer (1995) and Smits (1996). We derived the total abundances from deduced ionic abundances using the ionization correction factor (icf) formulae given by Kingsburgh & Barlow (1994)

$$\frac{\text{He}}{\text{H}} = \left(\frac{\text{He}^+}{\text{H}^+} + \frac{\text{He}^{2+}}{\text{H}^+} \right) \times \text{icf}(\text{He}), \text{icf}(\text{He}) = 1, \quad (2)$$

$$\frac{\text{O}}{\text{H}} = \left(\frac{\text{O}^+}{\text{H}^+} + \frac{\text{O}^{2+}}{\text{H}^+} \right) \times \text{icf}(\text{O}), \text{icf}(\text{O}) = \left(1 + \frac{\text{He}^{2+}}{\text{He}^+} \right)^{2/3}, \quad (3)$$

$$\frac{\text{N}}{\text{H}} = \left(\frac{\text{N}^+}{\text{H}^+} \right) \times \text{icf}(\text{N}), \text{icf}(\text{N}) = \left(\frac{\text{O}}{\text{O}^+} \right), \quad (4)$$

$$\frac{\text{Ne}}{\text{H}} = \left(\frac{\text{Ne}^{2+}}{\text{H}^+} \right) \times \text{icf}(\text{Ne}), \text{icf}(\text{Ne}) = \left(\frac{\text{O}}{\text{O}^{2+}} \right), \quad (5)$$

$$\frac{\text{S}}{\text{H}} = \left(\frac{\text{S}^+}{\text{H}^+} + \frac{\text{S}^{2+}}{\text{H}^+} \right) \times \text{icf}(\text{S}), \quad (6)$$

$$\text{icf}(\text{S}) = \left[1 - \left(1 - \frac{\text{O}^+}{\text{O}} \right)^3 \right]^{-1/3}, \quad (7)$$

Table 4. Diagnostic ratios for the electron temperature, T_e and the electron density, N_e .

Ion	Diagnostic	I.P. (eV)	Interior		Ring		Total	
			Ratio	T_e (10^3 K)	Ratio	T_e (10^3 K)	Ratio	T_e (10^3 K)
[N II]	$\frac{\lambda 6548 + \lambda 6584}{\lambda 5755}$	14.53	63.71:	11.76:	161.33	8.14	175.78	7.92
[O III]	$\frac{\lambda 4959 + \lambda 5007}{\lambda 4363}$	35.12	35.41::	$\lesssim 20.0$::	110.93	12.39	152.49	11.07
			Ratio	N_e (cm^{-3})	Ratio	N_e (cm^{-3})	Ratio	N_e (cm^{-3})
[S II]	$\frac{\lambda 6716}{\lambda 6731}$	10.36	2.02	$\lesssim 50.0$	1.46	$\lesssim 100.0$	1.51	$\lesssim 100.0$

$$\frac{\text{Ar}}{\text{H}} = \left(\frac{\text{Ar}^{2+}}{\text{H}^+} \right) \times \text{icf}(\text{Ar}), \text{icf}(\text{Ar}) = \left(1 - \frac{\text{N}^+}{\text{N}} \right)^{-1}. \quad (8)$$

We derived the ionic and total helium abundances from the observed $\lambda 5876$ and $\lambda 6678$, and He II $\lambda 4686$ ORLs. We assumed case B recombination for the singlet He I $\lambda 6678$ line and case A for other He I $\lambda 5876$ line (theoretical recombination models of Smits 1996). The He⁺/H⁺ ionic abundances from the He I lines at $\lambda 5876$ and $\lambda 6678$ were averaged with weights of 3:1, roughly the intrinsic intensity ratios of the two lines. The He²⁺/H⁺ ionic abundances were derived from the He II $\lambda 4686$ line using theoretical case B recombination rates from Storey & Hummer (1995). For high- and middle-EC PNe (EC >4), the total He/H abundance ratio can be obtained by simply taking the sum of singly and doubly ionized helium abundances, and with an icf(He) equal to or less than 1.0. For PNe with low levels of ionization, it is more than 1.0. SuWt 2 is an intermediate-EC PN (EC = 6.6; Dopita & Meatheringham 1990), so we can use an icf(He) of 1.0. We determined the O⁺/H⁺ abundance ratio from the [O II] $\lambda 3727$ doublet, and the O²⁺/H⁺ abundance ratio from the [O III] $\lambda 4959$ and $\lambda 5007$ lines. In optical spectra, only O⁺ and O²⁺ CELs are seen, so the singly and doubly ionized helium abundances deduced from ORLs are used to include the higher ionization stages of oxygen abundance.

We derived the ionic and total nitrogen abundances from [N II] $\lambda 6548$ and $\lambda 6584$ CELs. For optical spectra, it is possible to derive only N⁺, which mostly comprises only a small fraction (~ 10 – 30 per cent) of the total nitrogen abundance. Therefore, the oxygen abundances were used to correct the nitrogen abundances for unseen ionization stages of N²⁺ and N³⁺. Similarly, the total Ne/H abundance was corrected for undetermined Ne³⁺ by using the oxygen abundances. The $\lambda \lambda 6716, 6731$ lines usually detectable in PN are preferred to be used for the determination of S⁺/H⁺, since the $\lambda \lambda 4069, 4076$ lines are usually enhanced by recombination contribution, and also blended with O II lines. We notice that the $\lambda \lambda 6716, 6731$ doublet is affected by shock excitation of the ISM interaction, so the S⁺/H⁺ ionic abundance must be lower. When the observed S⁺ is not appropriately determined, it is possible to use the expression given by Kingsburgh & Barlow (1994) in the calculation, i.e. $(\text{S}^{2+}/\text{S}^+) = 4.677 + (\text{O}^{2+}/\text{O}^+)^{0.433}$.

The total abundances of He, N, O, Ne, S and Ar derived from our empirical analysis for selected regions of the nebula are given in Table 5. From Table 5 we see that SuWt 2 is a nitrogen-rich PN, which may be evolved from a massive progenitor ($M \geq 5$). However, the nebula's age (23 400–26 300 yr) cannot be associated with a faster evolutionary time-scale of a massive progenitor, since the evolutionary time-scale of $7 M_{\odot}$ calculated by Blöcker (1995) implies a short time-scale (less than 8000 yr) for the effective temperatures and the stellar luminosity (see Table 2) that are required to ionize the surrounding nebula. So, another mixing mechanism occurred during AGB nucleosynthesis, which further increased the nitrogen abundances in SuWt 2. Mass transfer to

Table 5. Ionic and total abundances deduced from the empirical analysis of the observed fluxes across different nebula regions of SuWt 2.

λ (Å)	Abundance	Interior	Ring	Total
5876	He ⁺ /H ⁺	–	0.066	0.049
6678	He ⁺ /H ⁺	0.031	0.057	0.043
Mean	He ⁺ /H ⁺	0.031	0.064	0.048
4686	He ²⁺ /H ⁺	0.080	0.027	0.036
	icf(He)	1.0	1.0	1.0
	He/H	0.111	0.091	0.084
6548	N ⁺ /H ⁺	7.932(–6)	1.269(–4)	1.284(–4)
6584	N ⁺ /H ⁺	1.024(–5)	1.299(–4)	1.334(–4)
Mean	N ⁺ /H ⁺	9.086(–6)	1.284(–4)	1.309(–4)
	icf(N)	16.240	2.014	3.022
	N/H	1.476(–4)	2.587(–4)	3.956(–4)
3727	O ⁺ /H ⁺	1.109(–5)	1.576(–4)	1.597(–4)
4959	O ²⁺ /H ⁺	6.201(–5)	8.881(–5)	1.615(–4)
5007	O ²⁺ /H ⁺	6.998(–5)	9.907(–5)	1.808(–4)
Mean	O ²⁺ /H ⁺	6.599(–5)	9.394(–5)	1.711(–4)
	icf(O)	2.336	1.262	1.459
	O/H	1.801(–4)	3.175(–4)	4.826(–4)
3869	Ne ²⁺ /H ⁺	2.635(–5)	9.608(–5)	1.504(–4)
3968	Ne ²⁺ /H ⁺	–	3.306(–5)	–
Mean	Ne ²⁺ /H ⁺	2.635(–5)	6.457(–5)	1.504(–4)
	icf(Ne)	2.728	3.380	2.820
	Ne/H	7.191(–5)	2.183(–4)	4.241(–4)
6716	S ⁺ /H ⁺	3.307(–7)	2.034(–6)	2.179(–6)
6731	S ⁺ /H ⁺	2.189(–7)	1.834(–6)	1.903(–6)
Mean	S ⁺ /H ⁺	2.748(–7)	1.934(–6)	2.041(–6)
6312	S ²⁺ /H ⁺	–	3.292(–8)	–
9069	S ²⁺ /H ⁺	3.712(–7)	1.198(–6)	1.366(–6)
Mean	S ²⁺ /H ⁺	3.712(–7)	6.155(–7)	1.366(–6)
	icf(S)	1.793	1.047	1.126
	S/H	1.158(–6)	2.668(–6)	3.836(–6)
7136	Ar ²⁺ /H ⁺	3.718(–7)	8.756(–7)	1.111(–6)
4740	Ar ³⁺ /H ⁺	–	–	4.747(–7)
7005	Ar ⁴⁺ /H ⁺	3.718(–7)	–	–
	icf(Ar)	1.066	1.986	1.494
	Ar/H	5.230(–7)	1.739(–6)	2.370(–6)

the two A-type companions may explain this typical abundance pattern.

Fig. 7 shows the spatial distribution of the ionic abundance ratio N⁺/H⁺, O⁺⁺/H⁺ and S⁺/H⁺ derived for given $T_e = 10\,000$ K and $N_e = 100 \text{ cm}^{-3}$. We notice that the O⁺⁺/H⁺ ionic abundance is very high in the inside shell, though the assumption of homogeneous electron temperature and density is not correct. The values in Table 5 are obtained using the mean T_e ([O III]) and N_e ([S II]) listed in Table 4. We notice that O²⁺/O⁺ = 5.9 for the interior

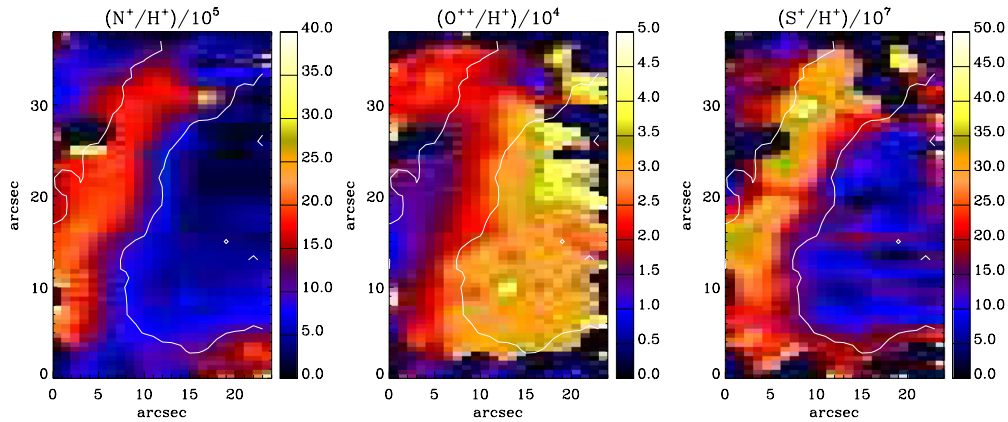


Figure 7. Spatial distribution maps of ionic nitrogen abundance ratio N^+/H^+ ($\times 10^{-5}$) from [N II] CELs (6548, 6584), ionic oxygen abundance ratio O^{++}/H^+ ($\times 10^{-4}$) from [O III] CELs (4959, 5007) and ionic sulphur abundance ratio S^+/H^+ ($\times 10^{-7}$) from [S II] CELs (6716, 6731) for $T_e = 10\,000\text{ K}$ and $N_e = 100\text{ cm}^{-3}$. The white contour lines show the distribution of the narrow-band emission of $H\alpha$ and [N II] in arbitrary units taken with the ESO 3.6 m telescope.

and $O^{2+}/O^+ = 0.6$ for the ring. Similarly, $He^{2+}/He^+ = 2.6$ for the interior and $He^{2+}/He^+ = 0.4$ for the ring. This means that there are many more ionizing photons in the inner region than in the outer region, which hints at the presence of a hot ionizing source in the centre of the nebula.

6 PHOTOIONIZATION MODEL

We used the 3D photoionization code `MOCASSIN` (version 2.02.67) to study the ring of the PN SuWt 2. The code, described in detail by Ercolano et al. (2003a, 2005, 2008), applies a Monte Carlo method to solve self-consistently the 3D radiative transfer of the stellar and diffuse field in a gaseous and/or dusty nebula having asymmetric/symmetric density distribution and inhomogeneous/homogeneous chemical abundances, so it can deal with any structure and morphology. It also allows us to include multiple ionizing sources located in any arbitrary position in the nebula. It produces several outputs that can be compared with observations, namely a nebular emission-line spectrum, projected emission-line maps, temperature structure and fractional ionic abundances. This code has already been used for a number of axisymmetric PNe, such as NGC 3918 (Ercolano et al. 2003b), NGC 7009 (Gonçalves et al. 2006), NGC 6781 (Schwarz & Monteiro 2006), NGC 6302 (Wright et al. 2011) and NGC 40 (Monteiro & Falceta-Gonçalves 2011). To save computational time, we began with the gaseous model of a $22 \times 22 \times 3$ Cartesian grid, with the ionizing source being placed in a corner in order to take advantage of the axisymmetric morphology used. This initial low-resolution grid helped us explore the parameter space of the photoionization models, namely ionizing source, nebula abundances and distance. Once we found the best-fitting model, the final simulation was done using a density distribution model constructed in $45 \times 45 \times 7$ cubic grids with the same size, corresponding to 14 175 cubic cells of length 1 arcsec each. Due to computational restrictions on time, we did not run any model with higher number of cubic cells. The atomic data set used for the photoionization modelling includes the CHIANTI data base (version 5.2; Landi et al. 2006), the improved coefficients of the H I, He I and He II free-bound continuous emission (Ercolano & Storey 2006) and the photoionization cross-sections and ionic ionization energies (Verner et al. 1993; Verner & Yakovlev 1995).

The modelling procedure consists of an iterative process during which the calculated $H\beta$ luminosity $L_{H\beta}$ (erg s^{-1}), the ionic abundance ratios (i.e. He^{2+}/He^+ , N^+/H^+ , O^{2+}/H^+) and the flux intensities of some important lines relative to $H\beta$ (such as He II $\lambda 4686$, [N II] $\lambda 6584$ and [O III] $\lambda 5007$) are compared with the observations. We performed a maximum of 20 iterations per simulation and the minimum convergence level achieved was 95 per cent. The free parameters included distance and stellar characteristics, such as luminosity and effective temperature. Although we adopted the density and abundances derived in Sections 4 and 5, we gradually scaled up/down the abundances in Table 5 until the observed emission-line fluxes were reproduced by the model. Due to the lack of infrared data, we did not model the dust component of this object. We notice however some variations among the values of $c(H\beta)$ between the ring and the inner region in Table 2. It means that that all of the observed reddening may not be due to the ISM. We did not include the outer bipolar lobes in our model, since the geometrical dilution reduces radiation beyond the ring. The faint bipolar lobes projected on the sky are far from the UV radiation field, and are dominated by the photodissociation region (PDR). There is a transition region between the photoionized region and PDR. Since `MOCASSIN` cannot currently treat a PDR fully, we are unable to model the region beyond the ionization front, i.e. the ring. This low-density PN is extremely faint, and not highly optically thick (i.e. some UV radiations escape from the ring), so it is difficult to estimate a stellar luminosity from the total nebula $H\beta$ intrinsic line flux. The best-fitting model depends upon the effective temperature (T_{eff}) and the stellar luminosity (L_*), though both are related to the evolutionary stage of the central star. Therefore, it is necessary to restrict our stellar parameters to the evolutionary tracks of the post-AGB stellar models, e.g. ‘late thermal pulse’, ‘very late thermal pulse’ (VLTP) or ‘asymptotic giant branch final thermal pulse’ (see e.g. Iben & Renzini 1983; Schönberner 1983; Vassiliadis & Wood 1994; Blöcker 1995; Herwig 2001; Miller Bertolami et al. 2006). To constrain T_{eff} and L_* , we employed a set of evolutionary tracks for initial masses between 1 and $7M_{\odot}$ calculated by Blöcker (1995, tables 3–5). Assuming a density model shown in Fig. 8, we first estimated the effective temperature and luminosity of the central star by matching the $H\beta$ luminosity $L(H\beta)$ and the ionic helium abundance ratio He^{2+}/He^+ with the values derived from observation and empirical analysis. Then, we scaled up/down abundances to get the best values for ionic abundance ratios and the flux intensities.

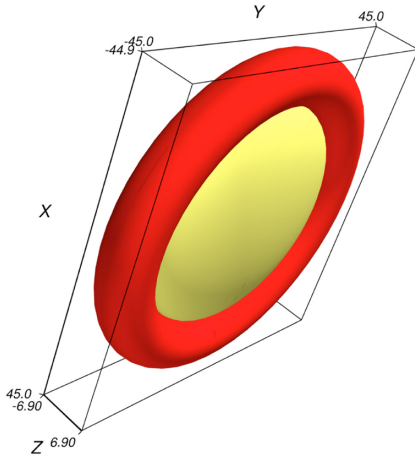


Figure 8. 3D isodensity plot of the dense torus adopted for photoionization modelling of SuWt 2. The torus has a homogeneous density of 100 cm^{-3} , a radius of 38.1 arcsec from its centre to the tube centre and a tube radius of 6.9 arcsec. The less dense oblate spheroid has a homogeneous density of 50 cm^{-3} , a semimajor axis of 31.2 arcsec and a semiminor axis of 6.9 arcsec. Axis units are arcsec, where 1 arcsec is equal to 1.12×10^{-2} pc based on the distance determined by our photoionization models.

6.1 Model input parameters

6.1.1 Density distribution

The dense torus used for the ring was developed from the higher spectral resolution kinematic model of Jones et al. (2010) and our plasma diagnostics (Section 4). Although the density cannot be more than the low-density limit of $N_e < 100 \text{ cm}^{-3}$ due to the [S II] $\lambda\lambda 6716/6731$ line ratio of $\gtrsim 1.40$, it was slightly adjusted to produce the total $H\beta$ Balmer intrinsic line flux $I(H\beta)$ derived for the ring and interior structure or the $H\beta$ luminosity $L(H\beta) = 4\pi D^2 I(H\beta)$ at the specified distance D . The three-dimensional density distribution used for the torus and interior structure is shown in Fig. 8. The central star is located in the centre of the torus. The torus has a radius of 38.1 arcsec from its centre to the centre of the tube (1 arcsec is equal to 1.12×10^{-2} pc based on the best-fitting photoionization models). The radius of the tube of the ring is 6.9 arcsec. The hydrogen number density of the torus is taken to be homogeneous and equal to $N_H = 100 \text{ cm}^{-3}$. Smith et al. (2007) studied similar objects, including SuWt 2, and found that the ring itself can be a swept-up thin disc, and the interior of the ring is filled with a uniform equatorial disc. Therefore, inside the ring, there is a less dense oblate spheroid with a homogeneous density of 50 cm^{-3} , a semimajor axis of 31.2 arcsec and a semiminor axis of 6.9 arcsec. The H number density of the oblate spheroid is chosen to match the total $L(H\beta)$ and be a reasonable fit for H^2+/H^+ compared to the empirical results. The dimensions of the model were estimated from the kinematic model of Jones et al. (2010) with an adopted inclination of 68° . The distance was estimated over a range 2.1–2.7 kpc, which corresponds to a reliable range based on the $H\alpha$ surface brightness–radius relation of Frew & Parker (2006) and Frew (2008). The distance was allowed to vary to find the best-fitting model. The value of 2.3 kpc adopted in this work yielded the best match to the observed $H\beta$ luminosity and it is also in very good agreement with Exter et al. (2010).

6.1.2 Nebular abundances

All major contributors to the thermal balance of the gas were included in our model. We used a homogeneous elemental abundance distribution consisting of eight elements. The initial abundances of He, N, O, Ne, S and Ar were taken from the observed empirically derived total abundances listed in Table 5. The abundance of C was a free parameter, typically varying between 5×10^{-5} and 8×10^{-3} in PNe. We initially used the typical value of $C/H = 5.5 \times 10^{-4}$ (Kingsburgh & Barlow 1994) and adjusted it to preserve the thermal balance of the nebula. We kept the initial abundances fixed while the stellar parameters and distance were being scaled to produce the best fit for the $H\beta$ luminosity and He^{2+}/He^+ ratio, and then we gradually varied them to obtain the finest match between the predicted and observed emission-line fluxes, as well as ionic abundance ratios from the empirical analysis.

The flux intensity of He II $\lambda 4686 \text{ \AA}$ and the He^{2+}/He^+ ratio highly depend on the temperature and luminosity of the central star. Increasing either T_{eff} or L_* or both increases the He^{2+}/He^+ ratio. Our method was to match the He^{2+}/He^+ ratio, and then scale the He/H abundance ratio to produce the observed intensity of He II $\lambda 4686 \text{ \AA}$.

The abundance ratio of oxygen was adjusted to match the intensities of [O III] $\lambda\lambda 4959, 5007$ and to a lesser degree [O II] $\lambda\lambda 3726, 3729$. In particular, the intensity of the [O II] doublet is unreliable due to the contribution of recombination and the uncertainty of about 30 per cent at the extreme blue of the WiFeS. So we gradually modified the abundance ratio O/H until the best match for [O III] $\lambda\lambda 4959, 5007$ and O^{2+}/H^+ was produced. The abundance ratio of nitrogen was adjusted to match the intensities of [N II] $\lambda\lambda 6548, 6584$ and N^+/H^+ . Unfortunately, the weak [N II] $\lambda 5755$ emission line does not have a high S/N ratio in our data.

The abundance ratio of sulphur was adjusted to match the intensities of [S III] $\lambda 9069$. The intensities of [S II] $\lambda\lambda 6716, 6731$ and S^+/H calculated by our models are about seven and ten times lower than those values derived from observations and empirical analysis, respectively. The intensity of [S II] $\lambda\lambda 6716, 6731$ is largely increased due to shock-excitation effects.

Finally, the differences between the total abundances from our photoionization model and those derived from our empirical analysis can be explained by the icf errors resulting from a non-spherical morphology and properties of the exciting source. Gonçalves et al. (2012) found that additional corrections are necessary compared to those introduced by Kingsburgh & Barlow (1994) due to geometrical effects. Comparison with results from photoionization models shows that the empirical analysis overestimated the neon abundances. The neon abundance must be lower than the value found by the empirical analysis to reproduce the observed intensities of [Ne III] $\lambda\lambda 3869, 3967$. It means that the icf(Ne) of Kingsburgh & Barlow (1994) overestimates the unseen ionization stages. Bohigas (2008) suggested to use an alternative empirical method for correcting unseen ionization stages of neon. It is clear that with the typical $Ne^{2+}/Ne = O^{2+}/O$ assumption of the icf method, the neon total abundance is overestimated by the empirical analysis.

6.1.3 Ionizing source

The central ionizing source of SuWt 2 was modelled using different non-local thermodynamic equilibrium (NLTE; Rauch 2003) model atmospheres listed in Table 6, as they resulted in the best fit of the nebular emission-line fluxes. Initially, we tested a set of blackbody fluxes with the effective temperature (T_{eff}) ranging from 80 000

Table 6. Parameters of the two best-fitting photoionization models. The initial mass, final mass and Post-AGB age are obtained from the evolutionary tracks calculated for hydrogen- and helium-burning models by Blöcker (1995).

	Nebula abundances		Stellar parameters	
Model 1	He/H	0.090	T_{eff} (kK)	140
	C/H	4.00(−4)	L_* (L_{\odot})	700
	N/H	2.44(−4)	$\log g$ (cgs)	7.0
	O/H	2.60(−4)	H : He	8 : 2
	Ne/H	1.11(−4)	M_* (M_{\odot})	~0.605
	S/H	1.57(−6)	M_{ZAMS} (M_{\odot})	3.0
	Ar/H	1.35(−6)	$\tau_{\text{post-AGB}}$ (yr)	7 500
Model 2	He/H	0.090	T_{eff} (kK)	160
	C/H	4.00(−4)	L_* (L_{\odot})	600
	N/H	2.31(−4)	$\log g$ (cgs)	7.3
	O/H	2.83(−4)	He : C : N : O	33 : 50 : 2 : 15
	Ne/H	1.11(−4)	M_* (M_{\odot})	~0.64
	S/H	1.57(−6)	M_{ZAMS} (M_{\odot})	3.0
	Ar/H	1.35(−6)	$\tau_{\text{post-AGB}}$ (yr)	25 000
Nebula physical parameters				
M_i/M_{\odot}	0.21	D (pc)	2 300	
N_{torus}	100 cm^{-3}	τ_{true} (yr)	23 400–26 300	
N_{spheroid}	50 cm^{-3}	[Ar/H]	−0.049	

to 190 000 K, the stellar luminosity compared to that of the Sun (L_*/L_{\odot}) ranging from 50 to 800 and different evolutionary tracks (Blöcker 1995). A blackbody spectrum provides a rough estimate of the ionizing source required to photoionize the PN SuWt 2. The assumption of a blackbody spectral energy distribution (SED) is not quite correct as indicated by Rauch (2003). The strong differences between a blackbody SED and a stellar atmosphere are mostly noticeable at energies higher than 54 eV (He II ground state). We thus successively used the NLTE Tübingen Model-Atmosphere Fluxes Package³ (TMAF; Rauch 2003) for hot compact stars. We initially chose the stellar temperature and luminosity (gravity) of the best-fitting blackbody model, and changed them to get the best observed ionization properties of the nebula.

Fig. 9 shows the NTLE model atmosphere fluxes used to reproduce the observed nebular emission-line spectrum by our photoionization models. We first used a hydrogen-rich model atmosphere with an abundance ratio of H : He = 8 : 2 by mass, $\log g = 7$ (cgs) and $T_{\text{eff}} = 140\,000$ K (Model 1), corresponding to the final stellar mass of $M_* = 0.605 M_{\odot}$ and the zero-age main sequence (ZAMS) mass of $M_{\text{ZAMS}} = 3 M_{\odot}$, where M_{\odot} is the solar mass. However, its post-AGB age ($\tau_{\text{post-AGB}}$) of 7500 yr, as shown in Fig. 10 (left-hand panel), is too short to explain the nebula's age. We therefore moved to a hydrogen-deficient model, which includes Wolf–Rayet central stars ([WC]) and the hotter PG 1159 stars. [WC]-type central stars are mostly associated with carbon-rich nebula (Zijlstra et al. 1994). The evolutionary tracks of the VLTP for H-deficient models, as shown in Fig. 10 (right-hand panel), imply a surface gravity of $\log g = 7.2$ for given T_{eff} and L_* . From the high temperature and high surface gravity, we decided to use ‘typical’ PG 1159 model atmosphere fluxes (He:C:N:O = 33:50:2:15) with $T_{\text{eff}} = 160\,000$ K and $L_*/L_{\odot} = 600$ (Model 2), corresponding to the post-AGB age of about $\tau_{\text{post-AGB}} = 25\,000$ yr, $M_* = 0.64 M_{\odot}$ and $M_{\text{ZAMS}} = 3 M_{\odot}$. The stellar mass found here is in agreement with the $0.7 M_{\odot}$ esti-

mate of Exter et al. (2010). Fig. 9 compares the two model atmosphere fluxes with a blackbody with $T_{\text{eff}} = 160\,000$ K.

Table 6 lists the parameters used for our final simulations in two different NTLE model atmosphere fluxes. The ionization structure of this nebula was best reproduced using these best two models. Each model has different effective temperature, stellar luminosity and abundances (N/H, O/H and Ne/H). The results of our two models are compared in Tables 7–10 to those derived from the observation and empirical analysis.

6.2 Model results

6.2.1 Emission-line fluxes

Table 7 compares the flux intensities calculated by our models with those from the observations. The fluxes are given relative to H β , on a scale where H β = 100. Most predicted line fluxes from each model are in fairly good agreement with the observed values and the two models produce very similar fluxes for most observed species. There are still some discrepancies in the few lines, e.g. [O II] $\lambda\lambda 3726, 3729$ and [S II] $\lambda\lambda 6716, 6731$. The discrepancies in [O II] $\lambda\lambda 3726, 3729$ can be explained by either recombination contributions or intermediate phase caused by a complex density distribution (see e.g. discussion in Ercolano et al. 2003c). [S II] $\lambda\lambda 6716, 6731$ was affected by shock ionization and its true flux intensity is much lower without the shock fronts. Meanwhile, [Ar III] 7751 was enhanced by the telluric line. The recombination lines H δ $\lambda 4102$ and He II $\lambda 5412$ were also blended with the O II recombination lines. There are also some recombination contributions in the [O II] $\lambda\lambda 7320, 7330$ doublet. Furthermore, the discrepancies in the faint auroral lines [N II] $\lambda 5755$ and [O III] $\lambda 4363$ can be explained by the recombination excitation contribution (see section 3.3 in Liu et al. 2000).

6.2.2 Temperature structure

Table 8 represents mean electron temperatures weighted by ionic abundances for Models 1 and 2, as well as the ring region and the inside region of the PN. We also see each ionic temperature corresponding to the temperature-sensitive line ratio of a specified ion. The definition for the mean temperatures was given in Ercolano et al. (2003b) and in detail by Harrington et al. (1982). Our model results for $T_e[\text{O III}]$ compare well with the value obtained from the empirical analysis in Section 4. Fig. 11 (top left) shows T_e obtained for Model 2 (adopted best-fitting model) constructed in $45 \times 45 \times 7$ cubic grids, and with the ionizing source being placed in the corner. It replicates the situation where the inner region has much higher T_e in comparison to the ring T_e as previously found by plasma diagnostics in Section 4. In particular, the mean values of $T_e[\text{O III}]$ for the ring (torus of the actual nebula) and the inside (spheroid) regions are around 12 000 and 15 000 K in all two models, respectively. They can be compared to the values of Table 4, that is $T_e[\text{O III}] = 12\,300$ K (ring) and $\lesssim 20\,000$ K (interior). Although the average temperature of $T_e[\text{N II}] \simeq 11\,700$ K over the entire nebula is higher than that given in Table 4, the average temperature of $T_e[\text{O III}] \simeq 13\,000$ K is in decent agreement with that found by our plasma diagnostics.

It can be seen in Table 4 that the temperatures for the two main regions of the nebula are very different, although we assumed a homogeneous elemental abundance distribution for the entire nebula relative to hydrogen. The temperature variations in the model can also be seen in Fig. 11. The gas density structure and the location

³ Website: <http://astro.uni-tuebingen.de/rauch/TMAF/TMAF.html>

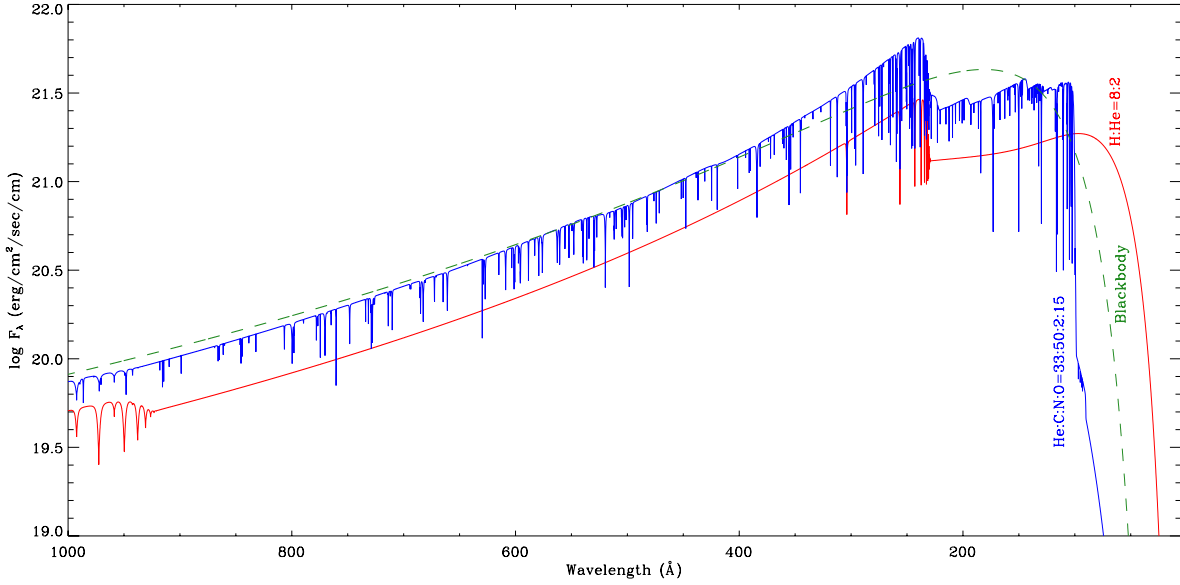


Figure 9. Comparison of two NLTE model atmosphere fluxes (Rauch 2003) used as ionizing inputs in our two models. Red line: H-rich model with an abundance ratio of H : He = 8:2 by mass, $\log g = 7$ (cgs) and $T_{\text{eff}} = 140\,000$ K. Blue line: PG 1159 model with He:C:N:O = 33:50:2:15, $\log g = 7$ and $T_{\text{eff}} = 160\,000$ K. Dashed green line: the flux of a blackbody with $T_{\text{eff}} = 160\,000$ K.

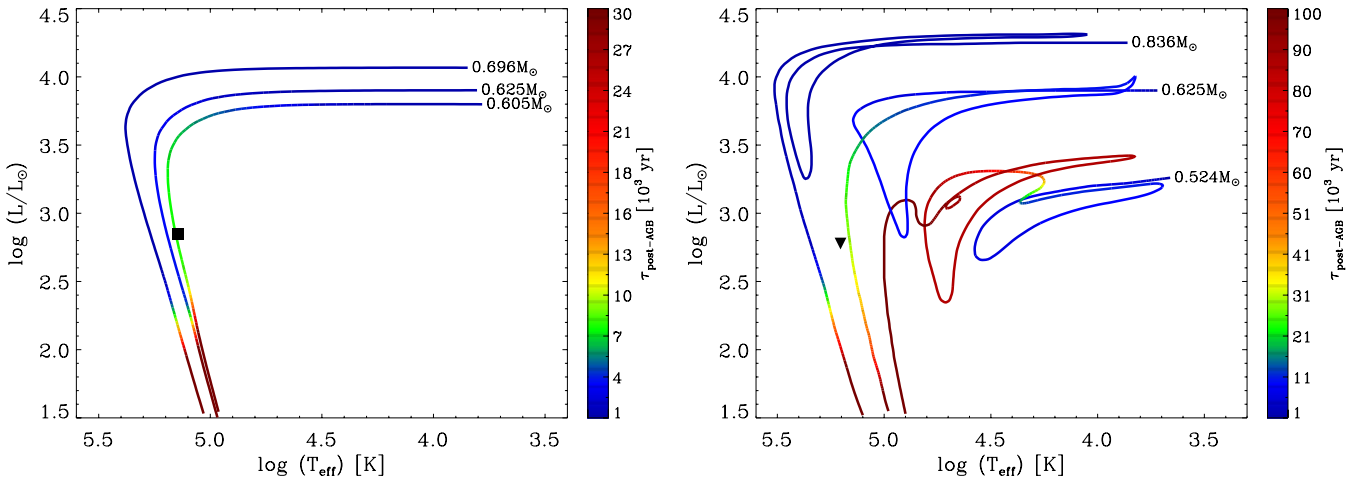


Figure 10. Hertzsprung–Russell diagrams for hydrogen-burning models (left-hand panel) with $(M_{\text{ZAMS}}, M_*) = (3 M_{\odot}, 0.605 M_{\odot})$, $(3 M_{\odot}, 0.625 M_{\odot})$ and $(4 M_{\odot}, 0.696 M_{\odot})$, and helium-burning models (right-hand panel) with $(M_{\text{ZAMS}}, M_*) = (1 M_{\odot}, 0.524 M_{\odot})$, $(3 M_{\odot}, 0.625 M_{\odot})$ and $(5 M_{\odot}, 0.836 M_{\odot})$ from Blöcker (1995) compared to the position of the central star of SuWt 2 derived from two different photoionization models, namely Model 1 (denoted by \blacksquare) and Model 2 (\blacktriangledown). On the right, the evolutionary tracks contain the first evolutionary phase, the VLTP (born-again scenario) and the second evolutionary phase. The colour scales indicate the post-AGB ages ($\tau_{\text{post-AGB}}$) in units of 10^3 yr.

of the ionizing source play a major role in heating the central regions, while the outer regions remain cooler as expected. Overall, the average electron temperature of the entire nebula increases by increasing the helium abundance and decreasing the oxygen, carbon and nitrogen abundances, which are efficient coolants. We did not include any dust grains in our simulation, although we note that a large dust-to-gas ratio may play a role in the heating of the nebula via photoelectric emissions from the surface of grains.

6.2.3 Ionization structure

Results for the fractional ionic abundances in the ring (torus) and inner (oblate spheroid) regions of our two models are shown in Table 9 and Fig. 11. It is clear from the figure and table that the

ionization structures from the models vary through the nebula due to the complex density and radiation field distribution in the gas. As shown in Table 9, He^{2+}/He is much higher in the inner regions, while He^+/He is larger in the outer regions, as expected. Similarly, we find that the higher ionization stages of each element are larger in the inner regions. From Table 9 we see that hydrogen and helium are both fully ionized, and neutrals are less than 8 per cent by number in these best-fitting models. Therefore, our assumption of $\text{icf}(\text{He}) = 1$ is correct in our empirical method.

Table 10 lists the nebular average ionic abundance ratios calculated from the photoionization models. The values that our models predict for the helium ionic ratio are fairly comparable with those from the empirical methods given in Section 5, though there are a number of significant differences in other ions. The O^+/H^+ ionic abundance ratio is about 33 per cent lower, while O^{2+}/H^+ is about

Table 9. Fractional ionic abundances for SuWt 2 obtained from the photoionization models. For each element, the upper row is for the torus (ring) and the lower row is for the oblate spheroid (inside).

Element	Ion							
	I	II	III	IV	V	VI	VII	
Model 1	H	6.53(-2)	9.35(-1)					
		3.65(-3)	9.96(-1)					
	He	1.92(-2)	7.08(-1)	2.73(-1)				
		3.05(-4)	1.27(-1)	8.73(-1)				
	C	5.92(-3)	2.94(-1)	6.77(-1)	2.33(-2)	1.86(-4)	7.64(-16)	1.00(-20)
		3.49(-5)	1.97(-2)	3.97(-1)	4.50(-1)	1.33(-1)	1.09(-12)	1.00(-20)
	N	7.32(-3)	4.95(-1)	4.71(-1)	2.62(-2)	4.18(-4)	6.47(-6)	2.76(-17)
		1.02(-5)	1.30(-2)	3.65(-1)	3.97(-1)	1.59(-1)	6.69(-2)	6.89(-13)
	O	6.15(-2)	4.98(-1)	4.21(-1)	1.82(-2)	7.09(-4)	1.34(-5)	7.28(-8)
		6.96(-5)	1.26(-2)	3.31(-1)	4.03(-1)	1.69(-1)	6.00(-2)	2.42(-2)
	Ne	3.46(-4)	6.70(-2)	9.10(-1)	2.26(-2)	3.56(-4)	4.25(-6)	2.11(-9)
		1.39(-6)	3.32(-3)	3.71(-1)	3.51(-1)	2.05(-1)	6.55(-2)	4.49(-3)
	S	1.13(-3)	1.67(-1)	7.75(-1)	5.52(-2)	1.15(-3)	6.20(-5)	8.53(-7)
		3.18(-6)	3.89(-3)	1.73(-1)	3.53(-1)	2.43(-1)	1.57(-1)	6.91(-2)
Ar	4.19(-4)	3.15(-2)	7.51(-1)	2.10(-1)	5.97(-3)	1.13(-3)	5.81(-5)	
	1.12(-7)	2.33(-4)	5.81(-2)	2.83(-1)	1.85(-1)	2.73(-1)	2.01(-1)	
Model 2	H	7.94(-2)	9.21(-1)					
		4.02(-3)	9.96(-1)					
	He	2.34(-2)	7.25(-1)	2.51(-1)				
		3.51(-4)	1.33(-1)	8.67(-1)				
	C	7.97(-3)	3.23(-1)	6.49(-1)	1.93(-2)	1.29(-4)	5.29(-16)	1.00(-20)
		4.45(-5)	2.23(-2)	4.13(-1)	4.41(-1)	1.23(-1)	1.00(-12)	1.00(-20)
	N	1.00(-2)	5.44(-1)	4.24(-1)	2.15(-2)	2.62(-4)	2.20(-6)	9.23(-18)
		1.31(-5)	1.52(-2)	3.84(-1)	4.07(-1)	1.50(-1)	4.40(-2)	4.34(-13)
	O	7.91(-2)	5.29(-1)	3.78(-1)	1.40(-2)	4.27(-4)	2.05(-6)	6.62(-11)
		9.34(-5)	1.50(-2)	3.60(-1)	4.20(-1)	1.75(-1)	2.97(-2)	1.85(-4)
	Ne	4.54(-4)	7.35(-2)	9.09(-1)	1.73(-2)	1.41(-4)	1.94(-8)	2.25(-14)
		1.75(-6)	3.85(-3)	4.19(-1)	3.86(-1)	1.89(-1)	1.73(-3)	6.89(-7)
	S	1.64(-3)	1.95(-1)	7.58(-1)	4.47(-2)	7.84(-4)	3.39(-5)	3.05(-7)
		4.23(-6)	4.86(-3)	1.96(-1)	3.61(-1)	2.39(-1)	1.47(-1)	5.16(-2)
Ar	7.22(-4)	3.99(-2)	7.74(-1)	1.81(-1)	3.95(-3)	5.62(-4)	1.60(-5)	
	1.72(-7)	3.22(-4)	7.30(-2)	3.30(-1)	1.96(-1)	2.62(-1)	1.39(-1)	

models for solar metallicity calculated by Ekström et al. (2012) imply that the A-type stars, both with masses close to $2.7 M_{\odot}$ and $T_{\text{eff}} \simeq 9200$ K, have ages of ~ 500 Myr. We see that they are in the evolutionary phase of the ‘blue hook’, a very short-lived phase just before the Hertzsprung gap. Interestingly, the initial mass of $3 M_{\odot}$ found for the ionizing source has the same age. As previously suggested by Exter et al. (2010), the PN progenitor with an initial mass slightly greater than $2.7 M_{\odot}$ can be coeval with the A-type stars, and it recently left the AGB phase. But, they adopted the system age of about 520 Myr according to the Y^2 evolutionary tracks (Yi, Kim & Demarque 2003; Demarque et al. 2004).

The effective temperature and stellar luminosity obtained for both models correspond to the progenitor mass of $3 M_{\odot}$. However, the strong nitrogen enrichment seen in the nebula is inconsistent with this initial mass, so another mixing process rather than the hot-bottom burning (HBB) occurs at substantially lower initial masses than the stellar evolutionary theory suggests for AGB phase (Herwig 2005; Karakas & Lattanzio 2007; Karakas et al. 2009). The stellar models developed by Karakas & Lattanzio (2007) indicate that HBB occurs in intermediate-mass AGB stars with the initial mass of $\geq 5 M_{\odot}$ for the metallicity of $Z = 0.02$, and $\geq 4 M_{\odot}$ for $Z = 0.004$ – 0.008 . However, they found that a low-metallicity AGB star ($Z = 0.0001$) with the progenitor mass of $3 M_{\odot}$ can also experience HBB. Our determination of the argon abundance in SuWt 2 (see

Table 6) indicates that it does not belong to the low-metallicity stellar population; thus, another non-canonical mixing process made the abundance pattern of this PN.

The stellar evolution also depends on the chemical composition of the progenitor, namely the helium content (Y) and the metallicity (Z), as well as the efficiency of convection (see e.g. Salaris & Cassisi 2005). More helium increases the H-burning efficiency, and more metallicity makes the stellar structure fainter and cooler. Any change in the outer layer convection affects the effective temperature. There are other non-canonical physical processes such as rotation, magnetic field and mass-loss during Roche lobe overflow (RLOF) in a binary system, which significantly affect stellar evolution. Ekström et al. (2012) calculated a grid of stellar evolutionary tracks with rotation, and found that N/H at the surface in rotating models is higher than non-rotating models in the stellar evolutionary tracks until the end of the central hydrogen- and helium-burning phases prior to the AGB stage. The Modules for Experiments in Stellar Astrophysics (MESA) code developed by Paxton et al. (2011, 2013) indicates that an increase in the rotation rate (or angular momentum) enhances the mass-loss rate. The rotationally induced and magnetically induced mixing processes certainly influence the evolution of intermediate-mass stars, which need further studies by MESA. The mass-loss in a binary or even triple system is much more complicated than a single rotating star, and many non-canonical physical

Table 10. Integrated ionic abundance ratios for the entire nebula obtained from the photoionization models.

Ionic ratio	Empirical	Model 1		Model 2	
		Abundance	Ionic fraction	Abundance	Ionic fraction
He ⁺ /H ⁺	4.80(−2)	5.308(−2)	58.97 per cent	5.419(−2)	60.21 per cent
He ²⁺ /H ⁺	3.60(−2)	3.553(−2)	39.48 per cent	3.415(−2)	37.95 per cent
C ⁺ /H ⁺	–	9.597(−5)	23.99 per cent	1.046(−4)	26.16 per cent
C ²⁺ /H ⁺	–	2.486(−4)	62.14 per cent	2.415(−4)	60.38 per cent
N ⁺ /H ⁺	1.309(−4)	9.781(−5)	40.09 per cent	1.007(−4)	43.58 per cent
N ²⁺ /H ⁺	–	1.095(−4)	44.88 per cent	9.670(−5)	41.86 per cent
N ³⁺ /H ⁺	–	2.489(−5)	10.20 per cent	2.340(−5)	10.13 per cent
O ⁺ /H ⁺	1.597(−4)	1.048(−4)	40.30 per cent	1.201(−4)	42.44 per cent
O ²⁺ /H ⁺	1.711(−4)	1.045(−4)	40.20 per cent	1.065(−4)	37.64 per cent
O ³⁺ /H ⁺	–	2.526(−5)	9.72 per cent	2.776(−5)	9.81 per cent
Ne ⁺ /H ⁺	–	6.069(−6)	5.47 per cent	6.571(−6)	5.92 per cent
Ne ²⁺ /H ⁺	1.504(−4)	8.910(−5)	80.27 per cent	9.002(−5)	81.10 per cent
Ne ³⁺ /H ⁺	–	1.001(−5)	9.02 per cent	1.040(−5)	9.37 per cent
S ⁺ /H ⁺ ^a	2.041(−6)	2.120(−7)	13.50 per cent	2.430(−7)	15.48 per cent
S ²⁺ /H ⁺	1.366(−6)	1.027(−6)	65.44 per cent	1.013(−6)	64.55 per cent
S ³⁺ /H ⁺	–	1.841(−5)	11.73 per cent	1.755(−7)	11.18 per cent
Ar ⁺ /H ⁺	–	3.429(−8)	2.54 per cent	4.244(−8)	3.14 per cent
Ar ²⁺ /H ⁺	1.111(−6)	8.271(−7)	61.26 per cent	8.522(−7)	63.13 per cent
Ar ³⁺ /H ⁺	4.747(−7)	3.041(−7)	22.52 per cent	2.885(−7)	21.37 per cent
Ar ⁴⁺ /H ⁺	–	5.791(−8)	4.29 per cent	5.946(−8)	4.40 per cent
Ar ⁵⁺ /H ⁺	–	7.570(−8)	5.61 per cent	7.221(−8)	5.35 per cent

^aShock excitation largely enhances the S⁺/H⁺ ionic abundance ratio.

parameters are involved (see e.g. BINSTAR code by Siess 2006; Siess et al. 2013). Chen & Han (2002) used the Cambridge stellar evolution (STARS) code developed by Eggleton (1971, 1972, 1973) to study numerically evolution of Population I binaries, and produced a helium-rich outer layer. Similarly, Benvenuto & De Vito (2003, 2005) developed a helium white dwarf from a low-mass progenitor in a close binary system. A helium enrichment in the outer layer can considerably influence other elements through the helium-burning mixing process.

7 CONCLUSION

In this paper, we have analysed new optical integral-field spectroscopy of the PN SuWt 2 to study detailed ionized gas properties, and to infer the properties of the unobserved hot ionizing source located in the centre of the nebula. The spatially resolved emission-line maps in the light of [N II] λ 6584 have described the kinematic structure of the ring. The previous kinematic model (Jones et al. 2010) allowed us to estimate the nebula's age and large-scale kinematics in the Galaxy. An empirical analysis of the emission-line spectrum led to our initial determination of the ionization structure of the nebula. The plasma diagnostics revealed as expected that the inner region is hotter and more excited than the outer regions of the nebula, and is less dense. The ionic abundances of He, N, O, Ne, S and Ar were derived based on the empirical methods and adopted mean electron temperatures estimated from the observed [O III] emission lines and electron densities from the observed [S II] emission lines.

We constructed photoionization models for the ring and interior of SuWt 2. This model consisted of a higher density torus (the ring) surrounding a low-density oblate spheroid (the interior disc). We assumed a homogeneous abundance distribution consisting of eight abundant elements. The initial aim was to find a model that could reproduce the flux intensities, thermal balance structure and

ionization structure as derived from by the observations. We incorporated NLTE model atmospheres to model the ionizing flux of the central star. Using a hydrogen-rich model atmosphere, we first fitted all the observed line fluxes, but the time-scale of the evolutionary track was not consistent with the nebula's age. Subsequently, we decided to use hydrogen-deficient stellar atmospheres implying a VLTP (born-again scenario), and longer time-scales were likely to be in better agreement with the dynamical age of the nebula. Although the results obtained by the two models of SuWt 2 are in broad agreement with the observations, each model has slightly different chemical abundances and very different stellar parameters. We found a fairly good fit to a hydrogen-deficient central star with a mass of $\sim 0.64 M_{\odot}$ with an initial (model) mass of $\sim 3 M_{\odot}$. The evolutionary track of Blöcker (1995) implies that this central star has a post-AGB age of about 25 000 yr. Interestingly, our kinematic analysis (based on v_{exp} from Jones et al. 2010) implies a nebular true age of about 23 400–26 300 yr.

Table 6 lists two best-fitting photoionization models obtained for SuWt 2. The hydrogen-rich model atmosphere (Model 1) has a normal evolutionary path and yields a progenitor mass of $3 M_{\odot}$, a dynamical age of 7500 yr and nebular N/O = 0.939 (by number). The PG 1159 model atmosphere (Model 2) is the most probable solution, which can be explained by a VLTP phase or born-again scenario: VLTP \rightarrow [WCL] \rightarrow [WCE] \rightarrow [WC]-PG 1159 \rightarrow PG 1159 (Blöcker 2001; Herwig 2001; Miller Bertolami & Althaus 2006; Werner & Herwig 2006). The PG 1159 model yields N/O = 0.816 and a stellar temperature of $T_{\text{eff}} = 160$ kK corresponding to the progenitor mass of $3 M_{\odot}$ and much longer evolutionary time-scale. The VLTP can be characterized as the helium-burning model, but this cannot purely explain the fast stellar winds ($V_{\infty} = 2000$ km s^{−1}) of typical [WCE] stars. It is possible that an external mechanism such as the tidal force of a companion and mass transfer to an accretion disc, or the strong stellar magnetic field of a companion, can trigger (late) thermal pulses during post-AGB evolution.

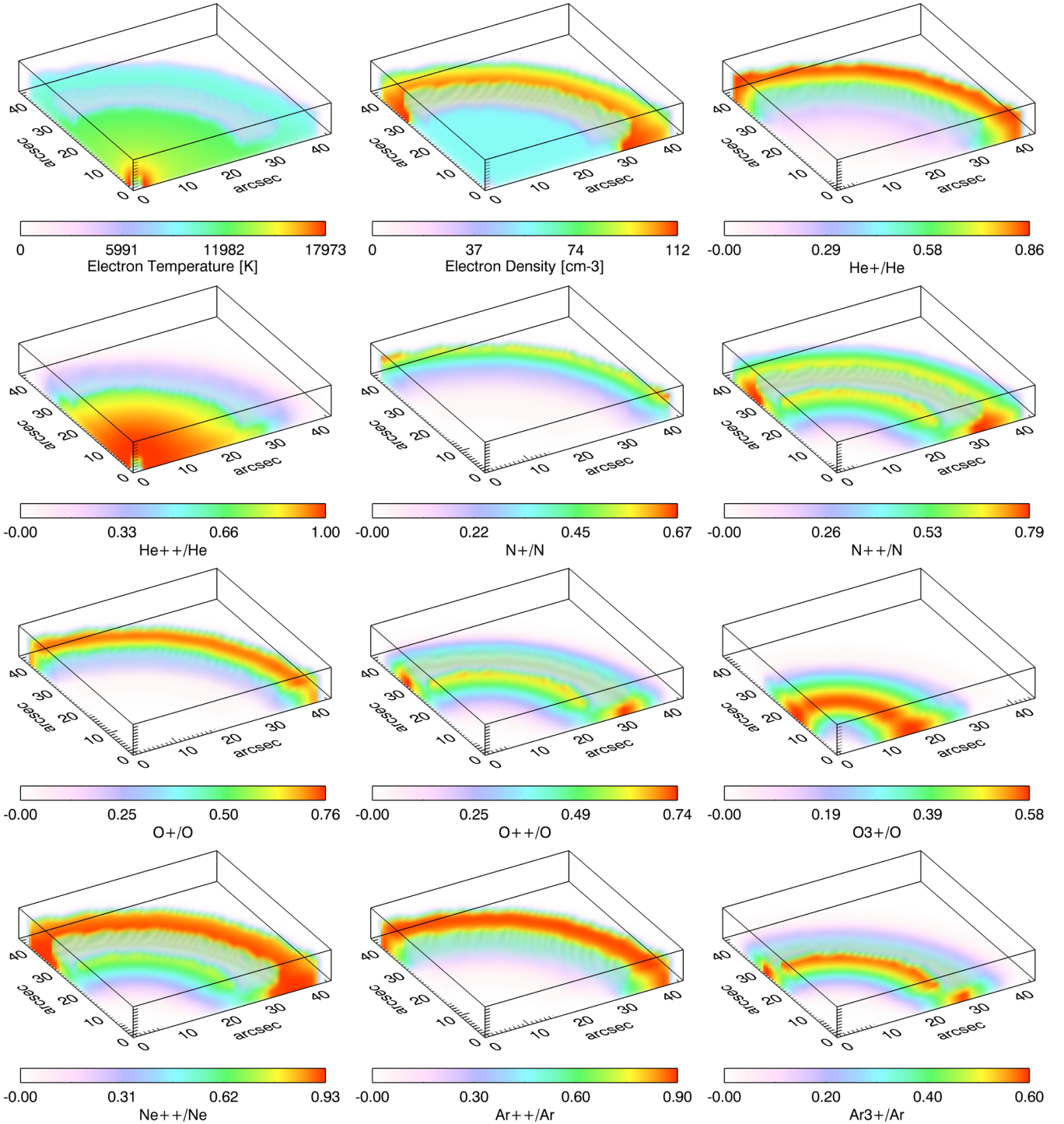


Figure 11. The 3D distributions of electron temperature, electron density and ionic fractions from the adopted Model 2 constructed in $45 \times 45 \times 7$ cubic grids, and the ionizing source being placed in the corner (0, 0, 0). Each cubic cell has a length of 1.12×10^{-2} pc, which corresponds to the actual PN ring size.

The abundance pattern of SuWt 2 is representative of a nitrogen-rich PN, which is normally considered to be the product of a relatively massive progenitor star (Becker & Iben 1980; Kingsburgh & Barlow 1994). Recent work suggests that HBB, which enhances helium and nitrogen, and decreases oxygen and carbon, occurs only for initial masses of $\geq 5 M_{\odot}$ ($Z = 0.02$; Karakas & Lattanzio 2007; Karakas et al. 2009); hence, the nitrogen enrichment seen in the nebula appears to result from an additional

mixing process active in stars down to a mass of $3 M_{\odot}$. Additional physical processes such as rotation increase the mass-loss rate (Paxton et al. 2013) and nitrogen abundance at the stellar surface (end of the core H- and He-burning phases; Ekström et al. 2012). The mass-loss via RLOF in a binary (or triple) system can produce a helium-rich outer layer (Chen & Han 2002; Benvenuto & De Vito 2005), which significantly affects other elements at the surface.

ACKNOWLEDGEMENTS

AD warmly acknowledges the award of an international Macquarie University Research Excellence Scholarship (iMQRES). QAP acknowledges support from Macquarie University and the Australian Astronomical Observatory. We wish to thank Nick Wright and Michael Barlow for interesting discussions. We are grateful to David J. Frew for the initial help and discussion. We thank Anna V. Kovacevic for carrying out the 2009 May 2.3 m observing run, and Lizette Guzman-Ramirez for assisting her with it. We also thank Travis Stenborg for assisting AD with the 2012 August 2.3 m observing run. AD thanks Milorad Stupar for his assistance in the reduction process. We would like to thank the staff at the ANU Siding Spring Observatory for their support, especially Donna Burton. This work was supported by the NCI National Facility at the ANU. We would also like to thank an anonymous referee for helpful suggestions that greatly improved the paper.

REFERENCES

- Aller L. H., Liller W., 1968, in Middlehurst B. M., Aller L. H., eds, Planetary Nebulae. University of Chicago Press, Chicago, p. 483
- Becker S. A., Iben I., Jr, 1980, *ApJ*, 237, 111
- Benvenuto O. G., De Vito M. A., 2003, *MNRAS*, 342, 50
- Benvenuto O. G., De Vito M. A., 2005, *MNRAS*, 362, 891
- Blöcker T., 1995, *A&A*, 299, 755
- Blöcker T., 2001, *Ap&SS*, 275, 1
- Bohigas J., 2008, *ApJ*, 674, 954
- Bond H. E., 2000, in Kastner J. H., Soker N., Rappaport S., eds, ASP Conf. Ser. Vol. 199, Asymmetrical Planetary Nebulae II: From Origins to Microstructures. Astron. Soc. Pac., San Francisco, p. 115
- Bond H. E., O'Brien M. S., Sion E. M., Mullan D. J., Exter K., Pollacco D. L., Webbink R. F., 2002, in Tout C. A., van Hamme W., eds, ASP Conf. Ser. Vol. 279, Exotic Stars as Challenges to Evolution. Astron. Soc. Pac., San Francisco, p. 239
- Bond H. E., Pollacco D. L., Webbink R. F., 2003, *AJ*, 125, 260
- Chen X., Han Z., 2002, *MNRAS*, 335, 948
- Demarque P., Woo J.-H., Kim Y.-C., Yi S. K., 2004, *ApJS*, 155, 667
- Dopita M. A., Meatheringham S. J., 1990, *ApJ*, 357, 140
- Dopita M. A., Meatheringham S. J., 1991, *ApJ*, 377, 480
- Dopita M. A. et al., 1996, *ApJ*, 460, 320
- Dopita M., Hart J., McGregor P., Oates P., Bloxham G., Jones D., 2007, *Ap&SS*, 310, 255
- Dopita M. et al., 2010, *Ap&SS*, 327, 245
- Eggleton P. P., 1971, *MNRAS*, 151, 351
- Eggleton P. P., 1972, *MNRAS*, 156, 361
- Eggleton P. P., 1973, *MNRAS*, 163, 279
- Ekström S. et al., 2012, *A&A*, 537, A146
- Ercolano B., Storey P. J., 2006, *MNRAS*, 372, 1875
- Ercolano B., Barlow M. J., Storey P. J., Liu X.-W., 2003a, *MNRAS*, 340, 1136
- Ercolano B., Morisset C., Barlow M. J., Storey P. J., Liu X.-W., 2003b, *MNRAS*, 340, 1153
- Ercolano B., Barlow M. J., Storey P. J., Liu X.-W., Rauch T., Werner K., 2003c, *MNRAS*, 344, 1145
- Ercolano B., Barlow M. J., Storey P. J., 2005, *MNRAS*, 362, 1038
- Ercolano B., Young P. R., Drake J. J., Raymond J. C., 2008, *ApJS*, 175, 534
- Exter K., Bond H. E., Pollacco D., Dufton P., 2003, in Kwok S., Dopita M., Sutherland R., eds, Proc. IAU Symp. 209, Planetary Nebulae: Their Evolution and Role in the Universe. Astron. Soc. Pac., San Francisco, p. 234
- Exter K., Bond H. E., Stassun K. G., Smalley B., Maxted P. F. L., Pollacco D. L., 2010, *AJ*, 140, 1414
- Frew D. J., 2008, PhD thesis, Department of Physics, Macquarie University
- Frew D. J., Parker Q. A., 2006, in Barlow M. J., Méndez R. H., eds, Proc. IAU Symp. 234, Planetary Nebulae in Our Galaxy and Beyond. Cambridge Univ. Press, Cambridge, p. 49
- Frew D. J., Bojčić I. S., Parker Q. A., 2013a, *MNRAS*, 431, 2
- Frew D. J., Bojčić I. S., Parker Q. A., Pierce M. J., Gunawardhana M. L. P., Reid W. A., 2013b, *MNRAS*, preprint (arXiv:1303.4555)
- Gesicki K., Zijlstra A. A., 2000, *A&A*, 358, 1058
- Gonçalves D. R., Ercolano B., Carnero A., Mampaso A., Corradi R. L. M., 2006, *MNRAS*, 365, 1039
- Gonçalves D. R., Wesson R., Morisset C., Barlow M., Ercolano B., 2012, in Manchado A., Stanghellini L., Schoenberner D., eds, Proc. IAU Symp. 283, Planetary Nebulae: An Eye to the Future. Cambridge University Press, Cambridge, p. 144
- Harrington J. P., Seaton M. J., Adams S., Lutz J. H., 1982, *MNRAS*, 199, 517
- Herwig F., 2001, *Ap&SS*, 275, 15
- Herwig F., 2005, *ARA&A*, 43, 435
- Howarth I. D., 1983, *MNRAS*, 203, 301
- Howarth I. D., Adams S., 1981, Program EQUIB. University College London (Wesson R., 2009, Converted to FORTRAN 90)
- Hummer D. G., Storey P. J., 1987, *MNRAS*, 224, 801
- Iben I., Jr, Renzini A., 1983, *ARA&A*, 21, 271
- Jacoby G. H., Ferland G. J., Korista K. T., 2001, *ApJ*, 560, 272
- Jones D., Lloyd M., Mitchell D. L., Pollacco D. L., O'Brien T. J., Vaytet N. M. H., 2010, *MNRAS*, 401, 405
- Karakas A., Lattanzio J. C., 2007, *PASA*, 24, 103
- Karakas A. I., van Raai M. A., Lugaro M., Sterling N. C., Dinerstein H. L., 2009, *ApJ*, 690, 1130
- Kingsburgh R. L., Barlow M. J., 1994, *MNRAS*, 271, 257
- Landi E., Del Zanna G., Young P. R., Dere K. P., Mason H. E., Landini M., 2006, *ApJS*, 162, 261
- Liu X.-W., Storey P. J., Barlow M. J., Danziger I. J., Cohen M., Bryce M., 2000, *MNRAS*, 312, 585
- Markwardt C. B., 2009, in Bohlender D. A., Durand D., Dowler P., eds, ASP Conf. Ser. Vol. 411, Astronomical Data Analysis Software and Systems XVIII. Astron. Soc. Pac., San Francisco, p. 251
- Miller Bertolami M. M., Althaus L. G., 2006, *A&A*, 454, 845
- Miller Bertolami M. M., Althaus L. G., Serenelli A. M., Panei J. A., 2006, *A&A*, 449, 313
- Monteiro H., Falceta-Gonçalves D., 2011, *ApJ*, 738, 174
- Moré J., 1977, in Watson G. A., ed., Lecture Notes in Mathematics, Vol. 630, Numerical Analysis. Springer-Verlag, Berlin, p. 105
- Parker Q. A. et al., 2005, *MNRAS*, 362, 689
- Paxton B., Bildsten L., Dotter A., Herwig F., Lesaffre P., Timmes F., 2011, *ApJS*, 192, 3
- Paxton B. et al., 2013, preprint (arXiv:1301.0319)
- Rauch T., 2003, *A&A*, 403, 709
- Reid W. A., Parker Q. A., 2010, *Publ. Astron. Soc. Aust.*, 27, 187
- Reid M. J. et al., 2009, *ApJ*, 700, 137
- Roeser S., Demleitner M., Schilbach E., 2010, *AJ*, 139, 2440
- Salaris M., Cassisi S., 2005, *Evolution of Stars and Stellar Populations*. Wiley
- Schoenberner D., 1983, *ApJ*, 272, 708
- Schwarz H. E., Monteiro H., 2006, *ApJ*, 648, 430
- Schwarz H. E., Corradi R. L. M., Melnick J., 1992, *A&AS*, 96, 23
- Seaton M. J., 1979a, *MNRAS*, 187, 73p
- Seaton M. J., 1979b, *MNRAS*, 187, 785
- Siess L., 2006, *A&A*, 448, 717
- Siess L., Izzard R. G., Davis P. J., Deschamps R., 2013, *A&A*, 550, A100
- Smith N., Bally J., Walawender J., 2007, *AJ*, 134, 846
- Smits D. P., 1996, *MNRAS*, 278, 683
- Steffen W., López J. A., 2006, *RMxAA*, 42, 99
- Storey P. J., Hummer D. G., 1995, *MNRAS*, 272, 41
- Tylenda R., Siódmiak N., Górny S. K., Corradi R. L. M., Schwarz H. E., 2003, *A&A*, 405, 627
- van Dokkum P. G., 2001, *PASP*, 113, 1420
- Vassiliadis E., Wood P. R., 1994, *ApJS*, 92, 125

Verner D. A., Yakovlev D. G., 1995, *A&AS*, 109, 125
Verner D. A., Yakovlev D. G., Band I. M., Trzhaskovskaya M. B., 1993, *At. Data Nucl. Data Tables*, 55, 233
Werner K., Herwig F., 2006, *PASP*, 118, 183
Wesson R., Stock D. J., Scicluna P., 2012, *MNRAS*, 422, 3516
West R. M., 1976, *PASP*, 88, 896
Wright N. J., Barlow M. J., Ercolano B., Rauch T., 2011, *MNRAS*, 418, 370

Yi S. K., Kim Y.-C., Demarque P., 2003, *ApJS*, 144, 259
Zijlstra A. A., van Hoof P. A. M., Chapman J. M., Loup C., 1994, *A&A*, 290, 228

This paper has been typeset from a $\text{\TeX}/\text{\LaTeX}$ file prepared by the author.